Cell Stem Cell

Article

Human pluripotent stem cell-derived atrioventricular node-like pacemaker cells exhibit biological conduction bridge properties

Graphical abstract

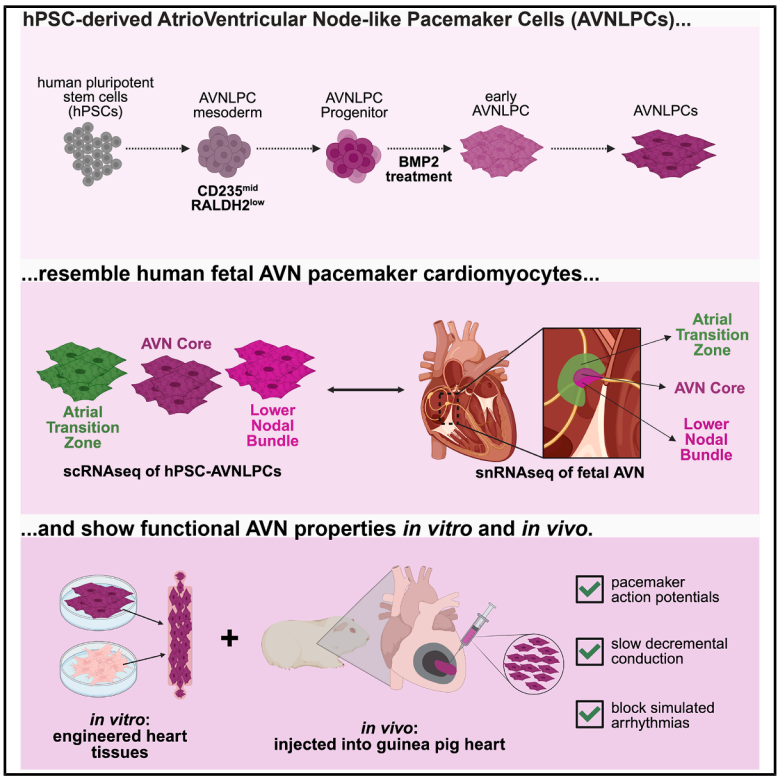

Highlights

- BMP signaling specifies cardiomyocyte progenitors into AVN-like pacemaker cells
- AVN-like pacemaker cells transcriptionally resemble fetal AVN cells
- Engineered tissues containing AVN-like pacemaker cells mimic AVN conduction
- AVN-like pacemaker cells display biological conduction bridge properties *in vivo*

Authors

Michelle Lohbihler, Amos A. Lim, Stéphane Massé, ..., Kumaraswamy Nanthakumar, Michael A. Laflamme, Stephanie Protze

Correspondence

stephanie.protze@uhn.ca

In brief

Protze and colleagues report a new protocol for the generation of human pluripotent stem cell-derived atrioventricular node-like pacemaker cells (AVNLPCs) via BMP signaling. These AVNLPCs display key AVN conduction properties upon engraftment into guinea pig hearts, representing a promising advancement toward a biological conduction bridge for the treatment of heart block.

Lohbihler et al., 2026, Cell Stem Cell *33*, 571–588
April 2, 2026
https://doi.org/10.1016/j.stem.2026.02.012

CellPress

Cell Stem Cell

CellPress
OPEN ACCESS

Article

Human pluripotent stem cell-derived atrioventricular node-like pacemaker cells exhibit biological conduction bridge properties

Michelle Lohbihler,[1,2] Amos A. Lim,[1,2] Stéphane Massé,[3,4] Brandon M. Murareanu,[1,2] Maggie Kwan,[1] Omar Mourad,[3,5] Olya Mastikhina,[3,5] Malak Elbatarny,[1,6,7] Renu Sarao,[1] Beiping Qiang,[1] Wahiba Dhahri,[1] Matthew L. Chang,[1,2] Alice L.Y. Xu,[1,2] Kasinan Suthiwanich,[3] Merrilyn Chen,[1,2] Amine Mazine,[1,5,7] Shahryar Khattak,[8,10] Sara S. Nunes,[3,5,6,9] Kumaraswamy Nanthakumar,[3,4] Michael A. Laflamme,[1,6] and Stephanie Protze[1,2,11,*]

[1]McEwen Stem Cell Institute, University Health Network, Toronto, ON M5G 1L7, Canada
[2]Department of Molecular Genetics, University of Toronto, Toronto, ON M5S 1A8, Canada
[3]Toronto General Hospital Research Institute, University Health Network, Toronto, ON M5G 1L7, Canada
[4]The Hull Family Cardiac Fibrillation Management Laboratory, University Health Network, Toronto, ON M5G 1L7, Canada
[5]Institute of Biomedical Engineering, University of Toronto, Toronto, ON M5S 3E3, Canada
[6]Department of Laboratory Medicine and Pathobiology, University of Toronto, Toronto, ON M5S 1A8, Canada
[7]Division of Cardiac Surgery, Department of Surgery, University of Toronto, Toronto, ON M5G 2C4, Canada
[8]Center for Commercialization of Regenerative Medicine (CCRM), Toronto, ON M5G 1M1, Canada
[9]Ajmera Transplant Centre, Peter Munk Cardiac Centre, University Health Network, Toronto, ON M5G 1L7, Canada
[10]Present address: King Abdullah University of Science and Technology, Thuwal 23955-6900, Saudi Arabia
[11]Lead contact
*Correspondence: stephanie.protze@uhn.ca
https://doi.org/10.1016/j.stem.2026.02.012

SUMMARY

The atrioventricular node (AVN) ensures synchronized heart contractions by establishing the electrical connection between the atria and ventricles. Dysfunction of the pacemaker cells of the AVN leads to atrioventricular block (AV block), a life-threatening condition managed with electronic pacemakers (EPMs). EPMs have drawbacks that could potentially be overcome by a human pluripotent stem cell (hPSC)-derived biological conduction bridge (BioCB). Recent studies demonstrated the differentiation of AVN-like cells from hPSCs, but their conduction properties upon engraftment *in vivo* remain unexplored. Here, we report the generation of AVN-like pacemaker cells (AVNLPCs) from hPSCs using Wnt and BMP signaling modulation. These AVNLPCs transcriptionally resemble fetal AVN pacemaker cells, exhibit pacemaker action potentials, and display unique AVN-like conduction properties. Notably, when transplanted into the guinea pig heart, AVNLPCs replicate the functional properties of the AVN. Our study highlights the potential of an AVNLPC-based BioCB as a novel cell therapy to improve treatment for patients with AV block.

INTRODUCTION

The atrioventricular node (AVN) plays a pivotal role as the electrical bridge between the atria and ventricles, ensuring synchronized heart contractions.[1–3] The AVN propagates electrical signals slower than the surrounding myocardium, establishing a delay that allows the ventricles to fill before contracting.[4–6] Additionally, the AVN blocks conduction of excessively fast atrial rates—for example, during atrial fibrillation—preventing life-threatening ventricular arrhythmias.[7–12] In cases of failure of the heart's primary pacemaker, the sinoatrial node (SAN),[13] the AVN acts as a backup pacemaker.[14]

Congenital or acquired AVN dysfunction disrupts electrical transmission, leading to atrioventricular block (AV block), associated with symptoms ranging from syncope to cardiac death. AV block is managed through the implantation of electronic pacemakers (EPMs), with ~1 million devices implanted annually.[15,16] While EPMs are lifesaving, they have inherent limitations, including the lack of autonomic regulation, recurrent surgical battery replacements, and the risk for complications including development of heart failure.[17–22] Therefore, there is a critical need to develop alternative therapies addressing the underlying cause of AVN dysfunction. A promising approach is the development of a human pluripotent stem cell (hPSC)-derived biological conduction bridge (BioCB) that can restore physiological conduction, providing a regenerative solution for AV block.

By recapitulating embryonic development, protocols have been established for the differentiation of hPSC-derived atrial-like cardiomyocytes (ALCMs), ventricular-like cardiomyocytes (VLCMs), and SAN-like pacemaker cells (SANLPCs).[23–29] The AVN develops from the atrioventricular canal (AVC), a transient embryonic structure between the atria and ventricles. AVC

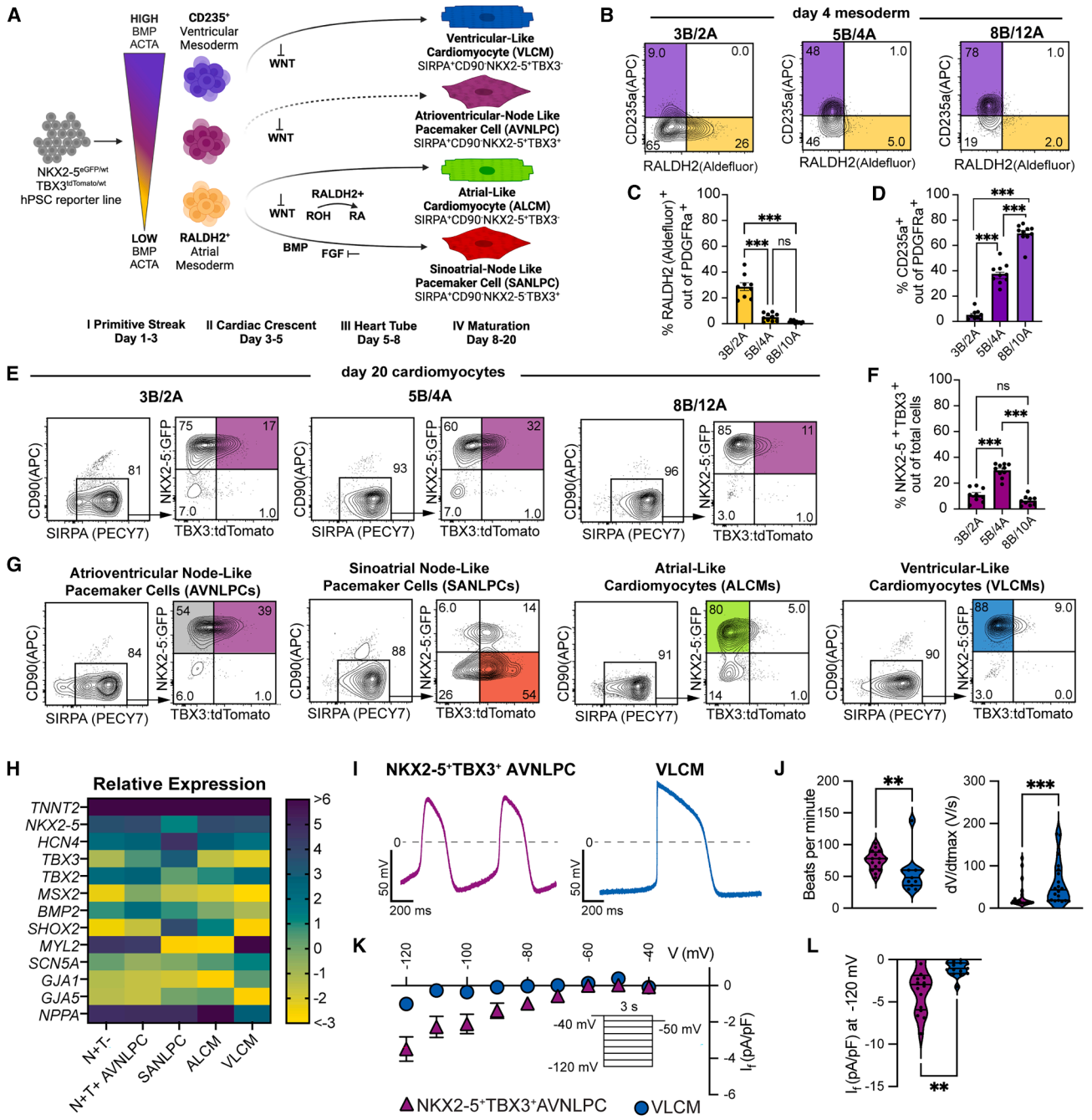

Figure 1. NKX2-5$^+$TBX3$^+$ cells represent AVNLPCs

(A) Summary of differentiation protocols. Dotted line: proposed AVNLPC lineage.

(B) Day 4 flow cytometric analysis of RALDH2 and CD235a expression. B, BMP4; A, activin A (ng/mL).

(C and D) Quantification of (C) RALDH2$^+$ and (D) CD235a$^+$ cells (n = 9–10).

(E) Day 20 flow cytometric analysis of NKX2-5:GFP and TBX3:tdTomato expression in SIPRA$^+$CD90$^-$ cardiomyocytes.

(F) Quantification of NKX2-5:GFP$^+$TBX3:Tdtomato$^+$ cardiomyocytes (n = 9–10).

(G) Gating strategy to isolate NKX2-5$^+$TBX3$^-$SIRPA$^+$CD90$^-$ cells (gray), NKX2-5$^+$TBX3$^+$SIRPA$^+$CD90$^-$ AVNLPCs (purple), NKX2-5$^-$TBX3$^+$SIRPA$^+$CD90$^-$ SANLPCs (red), NKX2-5$^+$TBX3$^-$SIRPA$^+$CD90$^-$ ALCMs (green), and NKX2-5$^+$TBX3$^-$SIRPA$^+$CD90$^-$ VLCMs (blue) at day 20.

(H) Heatmap of RT-qPCR gene expression profiles at day 20 (n = 9–11).

(I) Action potential traces of AVNLPCs and VLCMs.

(J) Quantification of action potential parameters. AVNLPCs: n = 16–20, VLCMs: n = 11–20 from three independent differentiations.

(legend continued on next page)

specification is driven by Wnt signaling, which induces downstream BMP signaling.[2,30–32] BMP signaling stimulates the expression of TBX2, MSX2, and TBX3, key transcription factors (TFs) required for AVN cardiomyocyte specification.[30,32,33] AVC cardiomyocytes either downregulate TBX3 and give rise to atrial and ventricular chamber cardiomyocytes or they maintain TBX3 expression and give rise to AVN pacemaker cells.[34,35] Notably, AVN pacemaker cells express NKX2-5, distinguishing them from SAN pacemaker cells.[36–38]

In the past 3 years, protocols utilizing Wnt or BMP signaling to differentiate hPSC-derived AVC-like cells have been reported.[39–42] These studies demonstrated that AVC-like cells slowly conduct electrical impulses. However, much remains to be learned about their properties and whether they can mimic the key functions of the native AVN. Furthermore, it is unknown how these cells will function *in vivo*, which is essential for the development of a BioCB.

Here, we generated a NKX2-5$^{eGFP/wt}$TBX3$^{tdTomato/wt}$ reporter hPSC line, enabling identification of AVN-like pacemaker cells (AVNLPCs). We demonstrate that activation of Wnt signaling using CHIR99021 induces BMP signaling, efficiently specifying AVNLPC fate from cardiac progenitors. Interestingly, direct activation of BMP signaling with BMP2 led to more efficient AVNLPC differentiation. These AVNLPCs transcriptionally match with fetal AVN cells and display pacemaker action potentials. We generated engineered heart tissues (EHTs) and demonstrated that AVNLPCs have slow, decremental conduction properties akin to the endogenous AVN. Using a guinea pig model, we were able to show that AVNLPCs maintain AVN-like conduction properties for up to 4 weeks after transplantation into the heart. Importantly only AVNLPCs, but not VLCMs, efficiently prevented the conduction of life-threatening arrhythmias, highlighting the importance of generating the appropriate cell type for a BioCB.

RESULTS

NKX2-5$^+$ TBX3$^+$ cells represent AVNLPCs

To identify NKX2-5$^+$TBX3$^+$ AVNLPCs in cardiac differentiations, we generated a NKX2-5$^{eGFP/wt}$TBX3$^{tdTomato/wt}$ HES3 reporter line[43] (Figures 1A and S1A–S1D). Because we previously showed that mesoderm specification impacts differentiation outcomes,[26] we aimed to identify mesoderm that most effectively generates AVNLPCs. We induced RALDH2$^+$ atrial mesoderm with 3 ng/mL BMP4 and 2 ng/mL activin A (3B/2A) and CD235a$^+$ ventricular mesoderm with 8B/12A, as previously described[26] (Figures 1B–1D). We included an intermediate induction using 5B/4A that resulted in mesoderm expressing 4.9% ± 1.0% RALDH2 and 37.7% ± 2.5% CD235. Notably, the 5B/4A mesoderm yielded the highest proportion of NKX2-5$^+$TBX3$^+$ cardiomyocytes (30.0% ± 1.7%; Figures 1E and 1F). To confirm that these NKX2-5$^+$TBX3$^+$ cells represent AVNLPCs, fluorescence-activated cell sorting (FACS) was used to isolate SIRPA$^+$ CD90$^-$NKX2-5$^+$TBX3$^+$ and SIRPA$^+$CD90$^-$NKX2-5$^+$TBX3$^-$ cardiomyocytes, and RT-qPCR was performed.[44] SANLPCs (SIRPA$^+$CD90$^-$NKX2-5$^-$TBX3$^+$), VLCMs, and ALCMs (SIRPA$^+$ CD90$^-$NKX2-5$^+$TBX3$^-$) were generated[26,28] as expression references (Figures 1G, 1H, S1E, and S1F). All populations expressed comparable levels of the cardiomyocyte marker *TNNT2*. As anticipated, NKX2-5$^+$TBX3$^+$ cells, VLCMs, and ALCMs expressed higher levels of NKX2-5 than SANLPCs. *TBX3* was significantly enriched in NKX2-5$^+$TBX3$^+$ cells and SANLPCs, compared with ALCMs, VLCMs, and NKX2-5$^+$ TBX3$^-$ cardiomyocytes. The pacemaker ion channel *HCN4* was expressed in NKX2-5$^+$TBX3$^+$ cells, although at lower levels than in SANLPCs. Importantly, the AVN markers *TBX2*, *BMP2*, *MSX2* were highly expressed in the NKX2-5$^+$ TBX3$^+$ cells, compared with the reference cells.[45] SAN (*SHOX2*), working cardiomyocyte (*SCN5A*), and ventricular (*MYL2*, *GJA1*), and atrial (*NPPA*, *GJA5*) markers were expressed at low levels in the NKX2-5$^+$TBX3$^+$ cells, compared with SANLPC, VLCM, and ALCM, respectively. Patch-clamp analysis showed that NKX2-5$^+$TBX3$^+$ cells have spontaneous beating rates of 75.4 ± 3.8 bpm, comparable to the human AVN[46,47] and significantly faster than VLCMs (Figures 1I, 1J, and S1G). NKX2-5$^+$TBX3$^+$ cells displayed pacemaker action potentials, with slower maximum upstroke velocities (dV/dtmax), compared with VLCMs,[28,48] while the diastolic membrane potentials were comparable likely due to the immature phenotype of the cells. In addition, NKX2-5$^+$TBX3$^+$ cells showed higher pacemaker funny currents (I_f) than VLCMs (Figures 1K and 1L). Altogether, NKX2-5$^+$TBX3$^+$ cardiomyocytes have the molecular and functional characteristics of AVN pacemaker cells and are referred to as AVNLPCs hereafter.

Wnt and BMP signaling guide AVNLPC differentiation

To promote differentiation of the 5B/4A mesoderm into AVNLPCs, we activated Wnt signaling using CHIR99021 (CHIR) in 4-day intervals during the heart tube to maturation stages (days 5–20) (Figure 2A). Wnt activation between days 8 and 18 significantly increased the proportion of AVNLPCs (Figures 2B and 2C). Earlier Wnt activation (days 5–8) disrupted cardiomyocyte differentiation. Using 12 μM CHIR between days 8 and 11 achieved the highest proportions of AVNLPCs (CHIR-AVNLPCs) (68.8% ± 4.1% out of total cells, 79.5% ± 3.6% out of SIRPA$^+$ CD90$^+$ cardiomyocytes) and a 1.5× increase in cell numbers (Figures 2D, 2E, S2A, and S2B). When we dissociated and reaggregated cells during treatment, 9 μM CHIR was sufficient to generate comparable AVNLPC proportions (Figure S2C). RT-qPCR immediately after CHIR treatment confirmed the upregulation of Wnt target (*AXIN2*, *LEF1*) and AVN (*TBX2*, *MSX2*, *TBX3*) genes (Figure S2D).

To investigate whether the CHIR effect is mediated by BMP signaling, we applied the BMP inhibitor LDN193189 (LDN) (Figures S2E and S2F). Addition of LDN, together with 12 μM CHIR, resulted in a significant reduction in AVNLPCs. RT-qPCR analysis confirmed that LDN inhibits the CHIR-induced

(K) I_f current-voltage relationship in AVNLPCs (n = 16) and VLCMs (n = 15).
(L) Maximum I_f current densities at −120 mV. Error bars represent SEM. One-way ANOVA (C, D, and F); Mann-Whitney test (J); unpaired t test (L): $^*p < 0.05$, $^{**}p < 0.01$, $^{***}p < 0.001$.
See also Figure S1.

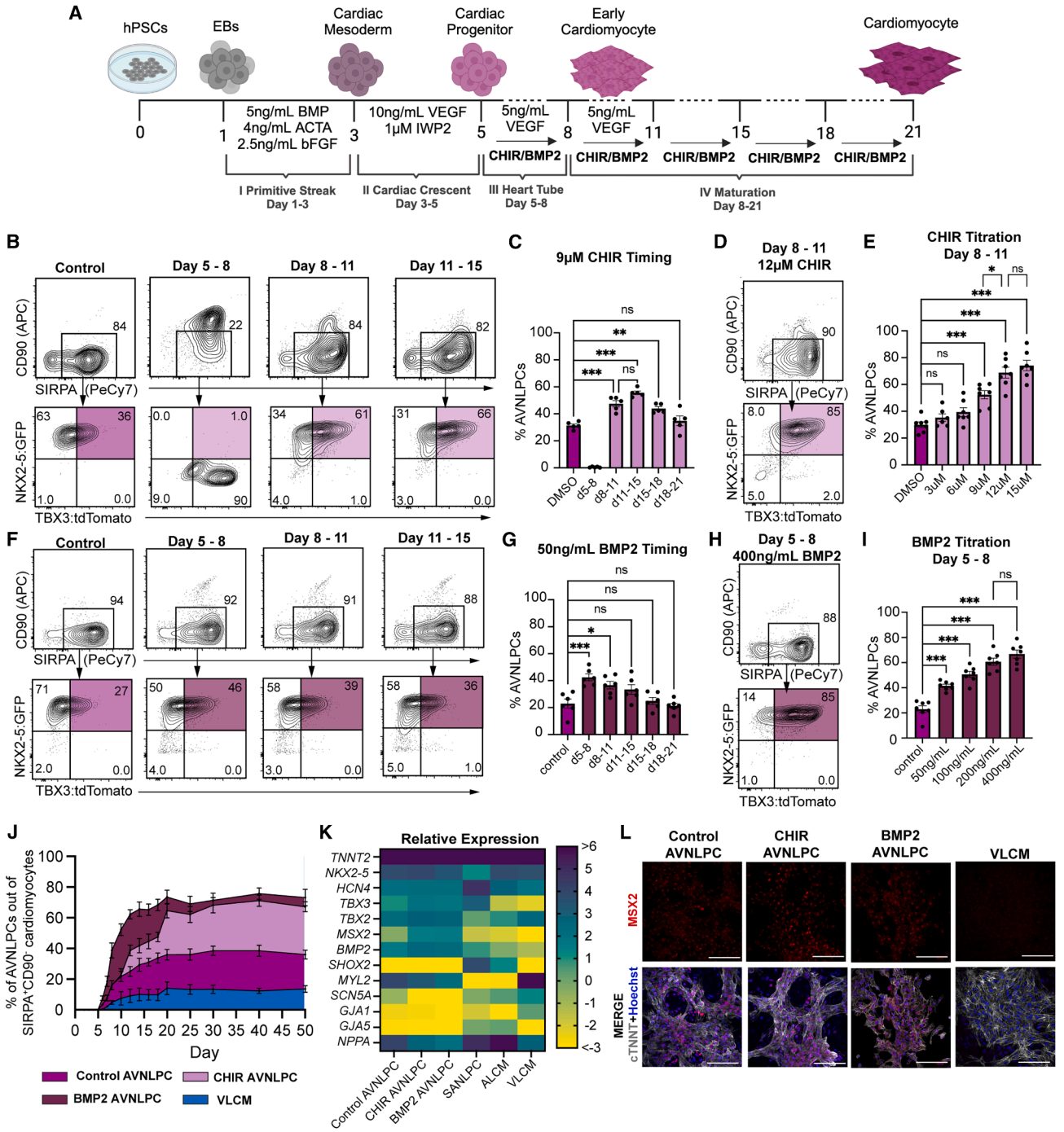

Figure 2. Wnt and BMP signaling guide AVNLPC differentiation

(A) Differentiation protocol indicating timing of CHIR/BMP2 treatment.

(B–I) Day 20 flow cytometric analysis of NKX2-5:GFP and TBX3:tdTomato expression in SIPRA^{+}CD90^{-} cardiomyocytes: (B) after treatment with 9 μM CHIR during the indicated time points and (C) quantification of AVNLPCs out of total cells (n = 5); (D) after treatment with 12 μM CHIR at days 8–11 and (E) quantification of AVNLPCs out of total cells after treatment with the indicated amounts of CHIR (n = 6–7); (F) after treatment with 50 ng/mL BMP2 during the indicated time points and (G) quantification of AVNLPCs out of total cells (n = 6); (H) after treatment with 400 ng/mL BMP2 at days 5–8 and (I) quantification of AVNLPCs out of total cells after treatment with the indicated amounts BMP2 (n = 7).

(J) Flow cytometric time course of the proportion of AVNLPCs.

(K) Heatmap of RT-qPCR gene expression profiles at day 20 (n = 7–9). Immunostaining of MSX2 and cTNT at day 20. Scale bars, 100 μm. Error bars represent SEM. One-way ANOVA: $^{*}p < 0.05$, $^{**}p < 0.01$, $^{***}p < 0.001$.

See also Figures S2 and S3.

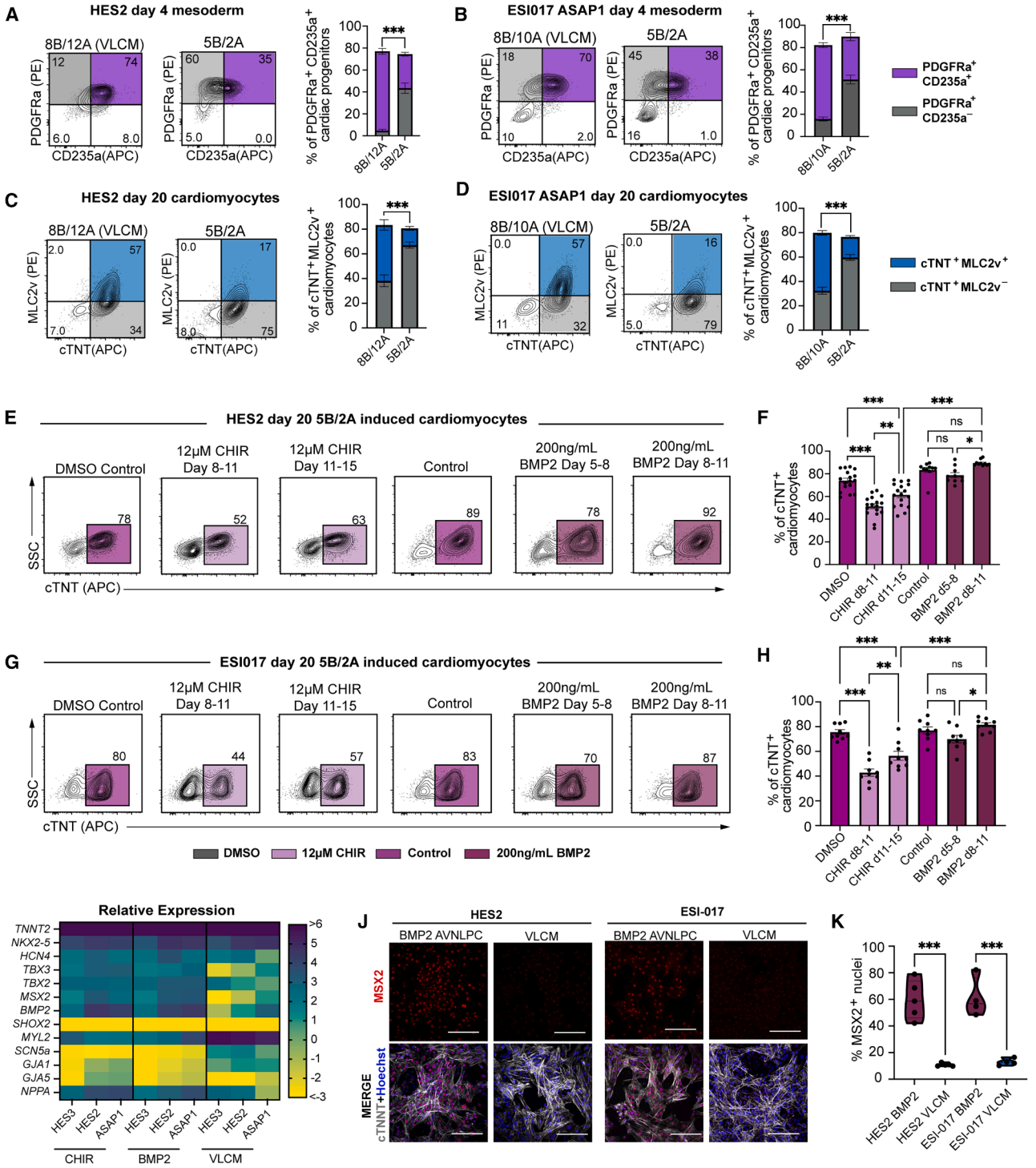

Figure 3. Generation of AVNLPCs from other hPSC lines

(A and B) Day 4 flow cytometric analysis of CD235a and PDGFRα expression in (A) the HES2 (n = 13) and (B) the ESI017-ASAP1 (n = 15) cell lines. B, BMP4; A, activin A (ng/mL).

(C and D) Day 20 flow cytometric analysis of cTNT and MLC2V expression in (C) the HES2 (n = 13) and (D) the ESI017-ASAP1 (n = 15) cell lines.

(E–H) Day 20 flow cytometric analysis for cTNT expression after treatment with 12 μM of CHIR or 200 ng/mL of BMP2: (E) in the HES2 cell line and (F) quantification (n = 10–17); (G) in the ESI-017-ASAP1 cell line and (H) quantification (n = 9).

(legend continued on next page)

upregulation of BMP target genes *ID1* and *ID2*, thereby blocking the upregulation of AVN genes (Figure S2D).

Based on these results, we tested the activation of BMP signaling to specify AVNLPCs. Addition of 400 ng/mL BMP2 from days 5 to 8 resulted in 66.8% ± 3.2% AVNLPCs (BMP2-AVNLPCs) (75.2% ± 3.4% out of cardiomyocytes), comparable to the CHIR-AVNLPC proportions (Figures 2F–2I and S2G). In contrast to CHIR-AVNLPCs, cell numbers were unchanged, and dissociation of cells during treatment did not reduce the required BMP2 concentration (Figures S2H and S2I). RT-qPCR immediately after BMP2 addition confirmed unchanged Wnt target gene and upregulated BMP target and AVN gene expression (Figure S2J). Finally, LDN treatment from days 5 to 8 abolished the baseline AVNLPC population observed in controls, indicating that their development is driven by endogenous BMP signaling (Figures S2J, S2K, and S2L).

Notch signaling prevents AVC specification in chamber myocardium.[49,50] Yet, inhibition of Notch signaling using L-685,458 (GSI) did not improve AVNLPC differentiation (Figure S2M).

Other AVC-like cardiomyocyte differentiation protocols[39,41,42] include retinoic acid (RA). Our 5B/4A mesoderm expressed low levels of RALDH2 (<5%), a marker of RA-dependent progenitors, and addition of RA reduced the proportion of AVNLPCs (Figure S2N). We therefore excluded RA from our protocol.

Time-course analysis showed that NKX2-5$^+$TBX3$^+$ cells emerged on day 6 and continuously increased until day 20, with the highest proportions observed in the CHIR- and BMP2-treated conditions (Figure 2J). The AVNLPC proportion remained high in the CHIR-AVNLPC and BMP2-AVNLPC samples and low in the control and VLCM samples until day 50, suggesting a stable phenotype.

To confirm the AVN phenotype of the CHIR- and BMP2-AVNLPCs, we FACS-isolated SIRPA$^+$CD90$^-$NKX2-5$^+$TBX3$^+$ cardiomyocytes and performed RT-qPCR (Figures 2K, S3A, and S3B). AVNLPCs from untreated controls, SANLPCs, ALCMs, and VLCMs were included as expression references. All samples expressed comparable levels of *TNNT2* and *NKX2-5*, except SANLPCs that had low NKX2-5 expression. *TBX3* expression was increased in CHIR-AVNLPCs and comparable to control-AVNLPCs in BMP2-AVNLPCs. Both CHIR- and BMP2-AVNLPCs displayed increased expression of *MSX2*, which was confirmed by immunostaining (Figure 2L). Expression of other marker genes was unchanged. Accordingly, beating rates of CHIR- and BMP2-AVNLPCs were comparable to control-AVNLPCs (Figure S3C).

Of note, combined BMP2 and CHIR (BMP2+CHIR) treatment did not further increase the proportion of AVNLPCs or the expression of AVN genes (Figures S3D–S3F). This is likely due to pathway redundancy, as Wnt signaling acts upstream of BMP2 during AVC specification. Collectively, these findings demonstrate that CHIR or BMP2 treatment is sufficient to specify AVNLPCs.

Generation of AVNLPCs from other hPSC lines

To evaluate its robustness, we applied the AVNLPC protocol to HES2 and ESI-017-ASAP1 hPSCs.[51,52] First, BMP4 and activin A were titrated to determine that 5B/2A results in ∼40% PDGFRa$^+$CD235a$^+$ mesoderm, matching the optimal mesoderm identified above (Figures 3A and 3B). Induction with higher cytokine concentrations (HES2: 8B/12A, ESI-017-ASAP1: 8B/10B) resulted in ventricular mesoderm expressing high levels of CD235a. Following Wnt inhibition, all mesoderms generated cardiomyocytes, with less MLC2v$^+$ cells obtained from the 5B/2A inductions (Figures 3C and 3D).

In contrast to the HES3 reporter hPSCs, treatment with CHIR and BMP2 had to be delayed by 3 days (days 11–15 and 8–11, respectively) to maintain high cardiomyocyte proportions (Figures 3E–3H). Of note, cardiomyocyte content was significantly higher in BMP2-AVNLPC compared with CHIR-AVNLPC cultures. To confirm AVNLPC phenotype, cardiomyocytes were isolated by magnetic-activated cell sorting (MACS) and analyzed by RT-qPCR. CHIR- and BMP2-AVNLPCs from the HES2 and ESI-017-ASAP1 hPSCs expressed AVN markers at comparable levels to the HES3-derived AVNLPCs and at higher levels than VLCMs (Figure 3I). Ventricular and atrial genes were expressed at low levels like in the HES3-derived AVNLPCs. Differentiation efficiency was quantified by MSX2 staining, showing 59.7% ± 6.5% and 61.1% ± 7.4% MSX2$^+$ BMP2-AVNLPCs for the HES2 and the ESI-017-ASAP1 hPSCs, respectively (Figures 3J and 3K).

Taken together, both protocols allow for the generation of AVNLPCs from multiple hPSC lines. Owing to the lower cardiomyocyte content in CIHR-AVNLPC cultures, we decided to focus subsequent experiments on BMP2-AVNLPCs.

Establishing a transcriptome expression reference of the fetal AVN

We performed single-nucleus RNA sequencing (snRNA-seq) of a 19-week gestation fetal heart to establish a AVN gene expression reference (Figure 4A). To increase the number of AVN cells in the sample, we specifically dissected the atrioventricular junction. Unsupervised clustering identified nine cell clusters, encompassing expected cell types, including non-cardiomyocytes and cardiomyocytes (Figure 4B; Tables S1 and S2). To resolve the complexity of the AVN, we subclustered the *TNNT2*$^+$ cardiomyocytes, resulting in 20 clusters (Figures S4A and S4B). Clusters were merged based on similarity in marker expression, identifying seven major cell types: core AVN; atrial transition zone (ATZ); lower nodal bundle (LNB); His bundle; and ventricular, atrial, and proliferating cardiomyocytes (Figures 4C and S4C; Table S2). Core AVN cells were identified by high expression of AVN (*RSPO3*, *MSX2*, *BMP2*, *TBX2*) and pacemaker (*TBX3*, *HCN4*, *GJC1*) genes (Figure 4D). They exhibited low expression of working cardiomyocyte genes (*GJA5*, *GJA1*, *SCN5A*) and were negative for SAN markers *SHOX2*, *CD34*, and *MYH11*.[53] The core AVN is surrounded by transitional cells with gradually

(I) Heatmap of RT-qPCR gene expression profiles across multiple hPSC lines at day 20.
(J) Immunofluorescent staining of MSX2 and cTNT at day 20. Scale bars, 100 μm.
(K) Quantification of MSX2$^+$ cells (n = 4–5 images per sample, from 4 to 5 independent differentiations). Error bars represent SEM. One-way ANOVA (F, H, and K); unpaired t test (A–D): $^*p < 0.05$, $^{**}p < 0.01$, $^{***}p < 0.001$.

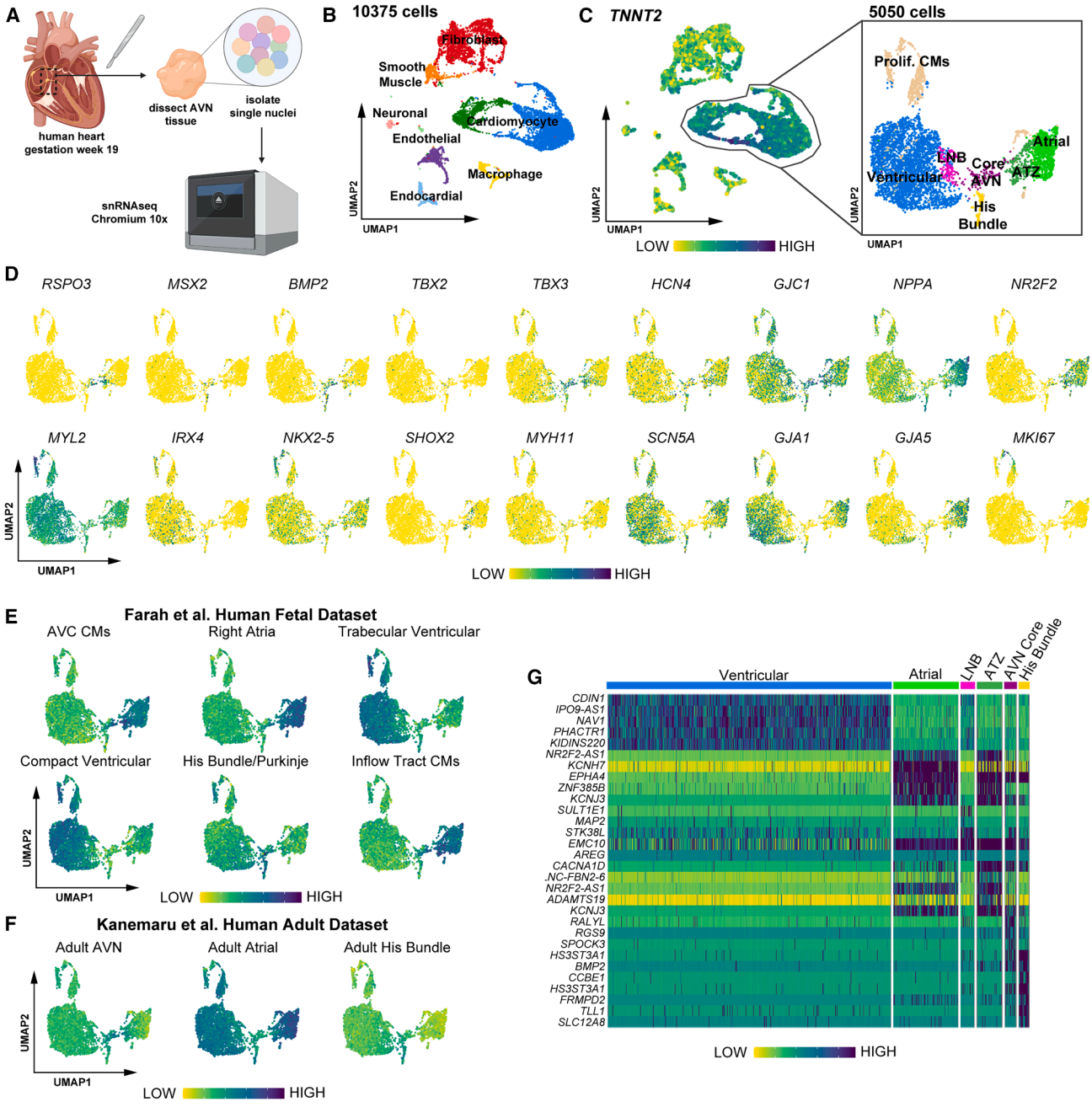

Figure 4. Single-nucleus transcriptomic profiling of the fetal AVN

(A) Sample preparation of AVN tissue.

(B) Uniform manifold approximation and projection (UMAP) of fetal AVN tissue.

(C) UMAPs depicting TNNT2^{+} clusters (left) and subclustered cardiomyocytes (right).

(D) UMAPs showing expression of the indicated genes.

(E and F) UMAPs showing signature score distribution for the DEGs of the indicated cell types from published datasets.

(G) Heatmap displaying the top five DEGs for each cardiomyocyte subcluster.

See also Figure S4 and Tables S1 and S2.

shifting gene expression. Accordingly, ATZ cells co-expressed AVN (*RSPO3*, *BMP2*, *TBX3*) and atrial (*NPPA*, *NR2F2*, *GJA5*) genes. Similarly, LNB cells expressed pacemaker (*TBX3*, *GJC1*) and ventricular (*MYL2*, *IRX4*) genes but low levels of working cardiomyocyte genes. The cluster expressing AVN markers, together with fast conducting ion channels *GJA5* and *SCN5A*, was annotated as the His bundle. Two atrial cell clusters were identified and merged based on the expression of *NPPA*, *GJA5*, *GJA1*, and *SCN5A*. Furthermore, nine ventricular clusters were identified and merged based on the expression of *MYL2*,

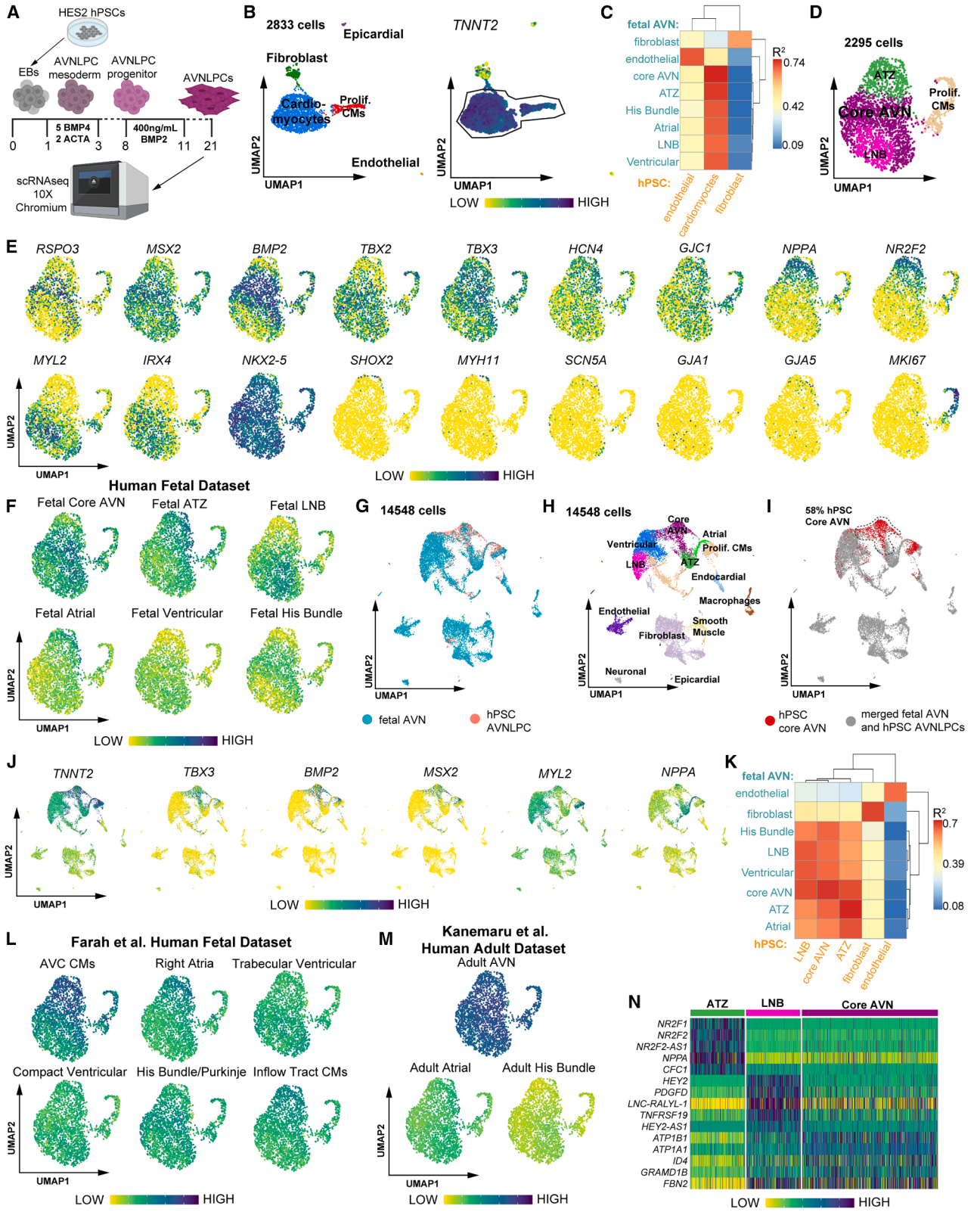

Figure 5. scRNA-seq of AVNLPCs reveals similarities to fetal AVN cardiomyocytes

(A) Differentiation protocol used for scRNA-seq.

(B) UMAPs of day 25 AVNLPCs (left) and TNNT2^{+} clusters (right).

(legend continued on next page)

IRX4, *GJA1*, and *SCN5A*. Lastly, five clusters of proliferating *MKI67*-expressing cells were identified.

Cell-type annotation was validated through gene signature scoring, using gene sets from a recent dataset of earlier human heart development (gestation weeks 9–15) by Farah et al. (Figures 4E and S4D).[54] The differentially expressed genes (DEGs) of the AVC cluster contained in this dataset scored the highest in our AVN and ATZ clusters, confirming our annotation. Similarly, the identity of our atrial, ventricular, and His bundle clusters were confirmed based on scoring with the DEGs of the respective subtypes from Farah et al.[54] In addition, DEGs from adult heart AVN cells identified by Kanemaru et al.[55] scored strongly with our fetal AVN cluster, supporting its identity (Figures 4F and S4E). Several of the DEGs identified in our core AVN cluster were also enriched in the Farah et al.[54] AVC cluster, including *RGS9*, *BMP2*, *TBX3*, and *RSPO3* (Figures 4G and S4F; Table S2). Finally, Gene Ontology (GO) analysis identified biological processes that further supported the AVN identity of the core AVN cluster (Figure S4G).

AVNLPCs resemble fetal core AVN pacemaker cells

Next, we performed single-cell RNA sequencing (scRNA-seq) of the hPSC-derived BMP2-AVNLPCs to assess their similarity to endogenous AVN cells (Figure 5A). As expected, most of the cells represented *TNNT2*$^+$ cardiomyocytes (Figure 5B; Tables S1 and S3). Spearman correlation analysis showed that these *TNNT2*$^+$ cells strongly correlate with the fetal core AVN (Figure 5C). The biological processes identified by GO analysis supported the AVN identity of the BMP2-AVNLPCs (Figure S4H).

To resolve cardiomyocyte subtypes, we subclustered the *TNNT2*$^+$ cells and identified seven clusters (Figures S4I and S4J). Clusters were merged based on similarity in marker gene expression, identifying four major cell types: AVN core, LNB, ATZ, and proliferating cardiomyocytes (Figures 5D and S4K; Table S3). Three clusters of core AVN cells were identified and merged based on the highest expression of AVN genes (*RSPO3*, *MSX2*, *BMP2*, *TBX2*) (Figure 5E). The ATZ and LNB clusters expressed lower levels of AVN genes, together with elevated levels of atrial (*NPPA*, *NR2F2*) and ventricular (*MYL2*, *IRX4*) markers, respectively. Finally, two clusters of proliferating cardiomyocytes were identified, marked by *MKI67* expression. None of the clusters expressed SAN or working cardiomyocyte markers, supporting an AVN-like phenotype. To validate the identity of these cell clusters, we performed gene signature scoring with the DEGs from our fetal dataset (Figures 5F and S4L). The fetal core AVN DEGs scored the highest in the hPSC core AVN cluster. Similarly, the DEGs from the fetal ATZ and LNB scored the highest in the hPSC ATZ and LNB clusters, respectively. Integration of the hPSC and fetal datasets showed that the majority of the hPSC core AVN cells (58%) cluster together with the fetal core AVN cells (Figures 5G–5J and S5A–S5C). Furthermore, Spearman correlation analysis demonstrated that the hPSC core AVN cells closely resemble fetal core AVN cells (Figure 5K).

We also compared the hPSC dataset with published fetal (Farah et al.[54]) and adult (Kanemaru et al.[55]) heart datasets (Figures 5L, 5M, S5D, and S5E). Fetal AVC cardiomyocyte DEGs scored the highest in our BMP2-AVNLPCs, while other cardiomyocyte subtypes resulted in lower scores. Similarly, adult heart AVN cell DEGs scored the highest in our BMP2-AVNLPCs, in contrast to low scores for atrial and His bundle DEGs. Finally, several of the DEGs in the hPSC core AVN cluster overlapped with DEGs of our fetal core AVN cluster, including *ATP1B1*, *ID4*, and *BMP2* (Figures 5N and S5F; Table S3). These analyses confirm the AVN identity of our BMP2-AVNLPCs and demonstrate that they contain core AVN and transitional cells like the fetal AVN. We next used pySCENIC to elucidate the gene regulatory networks underlying AVN cell identity, using both the fetal and hPSC-derived sn/scRNA-seq datasets (Figures S5G–S5J; Table S4).[56,57] Most interestingly, we identified a shared positive feedback loop between *TBX3* and *MSX2*, reinforcing AVN identity by driving expression of Wnt and BMP pathway (e.g., *BMP2*, *RSPO3*, *ID2*) and pacemaker-specific (e.g., *HCN4*, *CACNA1D*, *RGS6*) genes while suppressing working cardiomyocyte (e.g., *SCN5A*, *GJA1*, *GJA5*) genes.[2,33,58] Predicted upstream regulators of the MSX2-TBX3 axis included *SP3*, *PRDM6*, *FOXO1*, *ID4*, and *TBX2*. *SP3* and *PRDM6* are consistent with previously reported AVN regulatory network analyses,[59,60] whereas *FOXO1*, *ID4*, and *TBX2* have established roles relevant to the regulation of SCN5A, BMP signaling, and AVC development, respectively.[34,61–63]

Given multiple emerging protocols for generating hPSC-derived AVC/AVN-like cardiomyocytes, we compared how closely they recapitulate native AVN identity. Spearman correlation analysis of AVN-like cells from the CHIR- (Ye et al.),[40] WNT2- (Li et al.),[41] cardioid- (Schmidt et al.),[42] and our BMP2-based protocols showed that our AVNLPCs correlate most strongly with fetal core AVN cells, followed by cells from Li > Schmidt > Ye et al. (Figure S5K). A similar pattern was observed using adult AVN cells as a reference (Figure S5L).[55] Gene signature scoring using fetal and adult datasets confirmed this trend (Figure S5M).[54,55]

Engineered tissues containing AVNLPCs mimic conduction properties of the AVN

To assess the electrophysiological characteristics of AVNLPCs, we took advantage of the genetically encoded ASAP1 voltage

(C) Spearman correlation between fetal AVN and AVNLPC cell clusters.
(D) UMAP of subclustered *TNNT2*$^+$ cardiomyocytes.
(E) UMAPs showing expression of the indicated genes.
(F) UMAPs showing signature score distribution for the DEGs of fetal AVN cell types.
(G–I) UMAPs showing integration of the fetal AVN and AVNLPC datasets, labeled by (G) source dataset, (H) merged cell clusters, and (I) highlighting hPSC-derived core AVN cells.
(J) UMAPs showing expression of the indicated genes.
(K) Spearman correlation between fetal AVN and AVNLPC cell clusters.
(L and M) UMAPs showing signature score distribution for the DEGs of the indicated cell types from published datasets.
(N) Heatmap showing the top five DEGs for each AVNLPC subcluster.
See also Figures S4 and S5 and Tables S3 and S4.

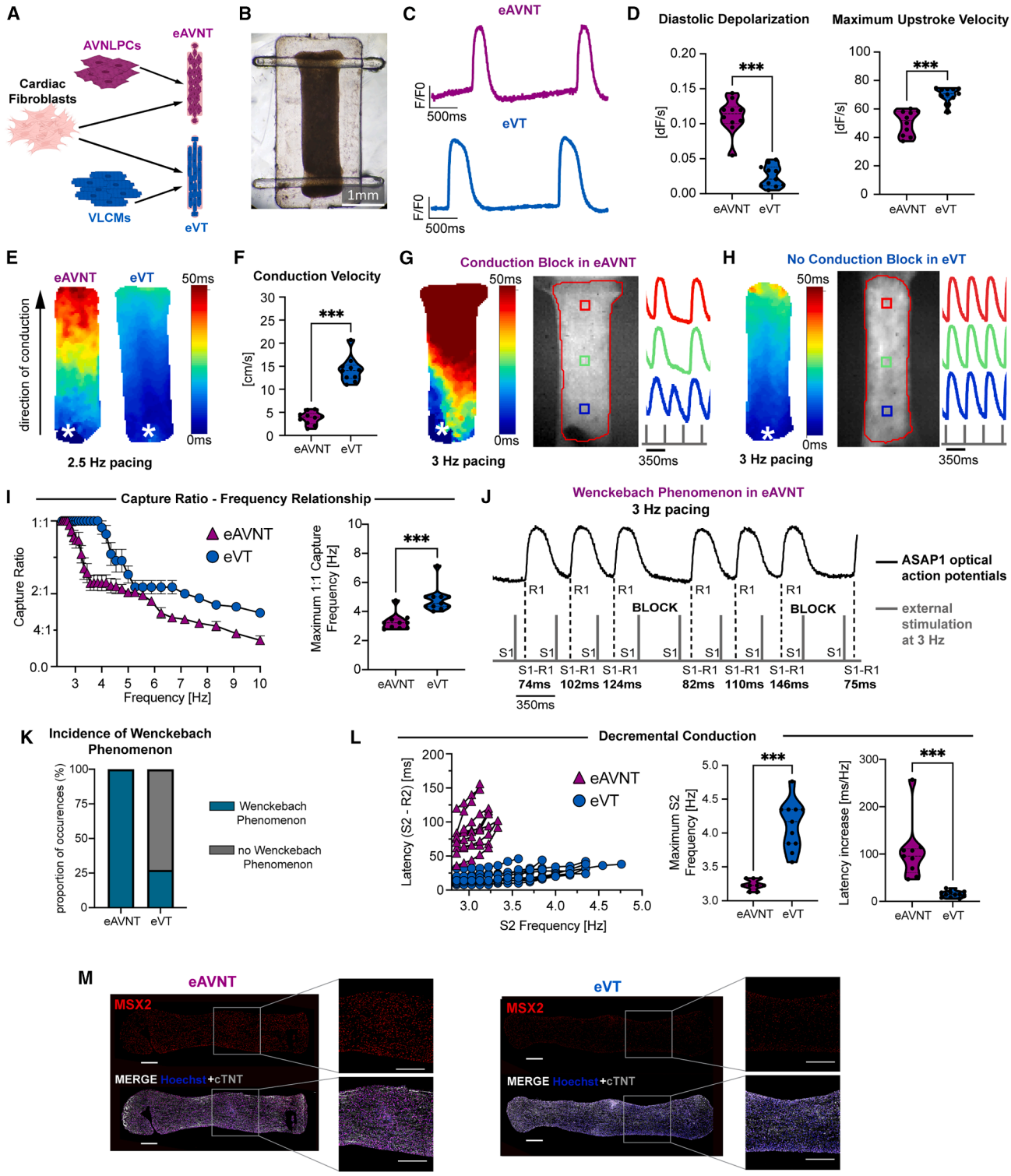

Figure 6. eAVNTs mimic conduction properties of the AVN

(A) Generation of eAVNT and eVT.

(B) Image of an eAVNT.

(C) Optical action potentials (oAPs) of an eAVNT and eVT.

(D) Quantification of oAP parameters in eAVNTs and eVTs.

(E) Voltage activation map of an eAVNT and eVT. Asterisk indicates pacing electrode.

(F) Quantification of conduction velocities.

(legend continued on next page)

sensor of the ESI-017-ASAP1 hPSCs.[51,64–66] AVNLPCs and VLCMs were isolated by MACS to achieve standardized cardiomyocyte contents (>80%) and seeded together with cardiac fibroblasts (3:1 ratio) into molds to make 3-mm-long engineered AVN tissues (eAVNTs) or ventricular tissues (eVTs), respectively (Figures 6A and 6B). eAVNTs had spontaneous beating rates of 37.9 ± 4.0 bpm, which were significantly faster than those of eVTs but slower than those of AVNLPC aggregates, most likely due to the electrical load of the fibroblasts included in the tissues (Figure S6A). As expected for pacemaker cells, spontaneous action potentials of eAVNTs showed significantly faster diastolic depolarization and significantly slower maximum action potential upstroke velocities, compared with eVTs (Figures 6C, 6D, and S6B). Since the AVN acts as a conduction bridge between the atria and ventricles, we next analyzed conduction properties at 2.5 Hz pacing (Figures 6E and 6F). Conduction velocities in eAVNTs were significantly slower than in eVTs (3.8 ± 0.4 vs. 14.5 ± 0.8 cm/s) and comparable to the human AVN.[1,67] To test for the important function of the AVN to block conduction of fast atrial rhythms, we gradually increased the pacing frequency (Figures 6G–6I). eAVNTs showed 1:1 capture until 3.2 ± 0.2 Hz. At higher frequencies, eAVNTs transitioned into 2:1 and eventually 4:1 conduction block. In contrast, eVTs showed 1:1 capture up to 4.6 ± 0.2 Hz, indicating that AVNLPCs more effectively block fast rhythms. We next assessed the mechanisms underlying these conduction properties. 100% of eAVNTs exhibited the Wenckebach phenomenon, defined as a progressive increase in impulse conduction time (S1-R1) at a fixed stimulation frequency (S1-S1), leading up to a blocked beat[8,9] (Figures 6J and 6K). This phenomenon is a hallmark of AVN tissue and is not observed in healthy ventricular tissue. Accordingly, the majority of eVTs (73%) did not display the Wenckebach phenomenon (Figure S6C). We next assessed whether eAVNTs show decremental conduction like the endogenous AVN[11,12] (Figures 6L and S6D–S6F). We used a S1-S2 protocol consisting of eight stimuli at a stable frequency (S1, 2.5 Hz), followed by a premature stimulation with increasing frequency (S2, 3–10 Hz).[68–70] Tissues were paced from the bottom, and action potentials were detected at the top. In eAVNTs, the time from S2 stimulation to activation of the R2 action potential (latency) increased with increasing S2 frequency until conduction of the S2 stimulation was blocked. eVTs also displayed a frequency-dependent increase in latency. However, based on the slope of the latency increase, decremental conduction in eAVNTs was stronger. These results were confirmed using the NKX2.5$^{eGFP/wt}$TBX3$^{tdTomato/wt}$ HES3 line (Figures S6G–S6I).

To determine whether differences in cell survival or composition contributed to these functional differences, we performed histological analysis (Figures 6M and S6J–S6N). Immunostaining for cTNT, NKX2-5, MSX2, and Vimentin (fibroblasts) confirmed the molecular identity of MSX2^{+} eAVNTs and MSX2^{low} eVTs and showed no differences in cellular composition. Comparable low levels of cell death and proliferation were detected in eAVNTs and eVTs. Together, these data demonstrate that AVNLPCs mimic key electrophysiological properties of the AVN.

AVNLPCs exhibit AVN conduction properties *in vivo*

Initially, we attempted to determine the ability of AVNLPCs to act as a BioCB between the atria and ventricle by suturing eAVNTs into the guinea pig AV groove and inducing AV block *ex vivo* 2 weeks post-transplantation. This approach failed due to poor electrical integration of the tissue grafts with the host heart (3 of 30 animals, data not shown), consistent with other reports.[71–74] We therefore transitioned to injecting AVNLPCs into cryoinjured guinea pig hearts that served as a defined platform for testing their conduction properties *in vivo*[51,75] (Figure 7A). First, we created scar tissue using cryoinjury to establish an artificial conduction block in the left ventricle. After 10 days, 80–100 million ESI-017-ASAP1-dervied AVNLPCs or VLCMs were injected spanning from the healthy myocardium into the scar. This approach enabled assessment of conduction properties of the grafts within the insulated scar, minimizing interference from host myocardium. Then, 2–4 weeks post-transplantation, hearts were harvested and mounted to a Langendorff perfusion system enabling *ex vivo* electrocardiogram (ECG) recording and optical mapping. Electric activity of the grafts was measured using ASAP1, while host activity was measured using perfusion with the voltage-sensitive dye RH237 (Figures 7B, 7C, and S7A).[75,76] The host SAN and AVN were suppressed using methacholine, allowing for control of the ventricular rate with a pacing electrode (Figures 7A and S7B–S7D). At 2 Hz, action potentials from the AVNLPC and VLCM grafts and the host hearts were synchronized and aligned with the heart's ECG, indicating that the grafts are electrically coupled with the host[77] (n = 4 of 6/7 of 8 animals for AVNLPCs/VLCMs; Figures 7D and 7F).

Since the AVN is the secondary pacemaker, we evaluated whether AVNLPCs can pace the host hearts[78] (Figure 7E). When we ceased electrical pacing, all four animals with electrically coupled AVNLPC grafts displayed sustained ectopic beats, suggesting the grafts were pacing the ventricle. ECG recordings (change in direction) and voltage activation maps (change in signal origin) confirmed that the ectopic beats originated from the grafts. In contrast, only two of seven animals with electrically coupled VLCM grafts displayed sustained ectopic pacing (Figures 7G and 7H). Consistently, the AVNLPC grafts exhibited pacemaker action potentials with diastolic depolarization and slower maximum upstroke velocity than VLCM grafts (Figures 7I and S7E).

(G and H) Voltage activation maps, and oAPs of (G) an eAVNT and (H) an eVT at 3 Hz pacing. Asterisk indicates pacing electrode.
(I) Capture ratios of eAVNTs and eVTs at increasing pacing frequencies (left). Frequency at which 1:1 capture is lost (right).
(J) Wenckebach phenomenon in an eAVNT. S1, pacing stimulus; S1-R1, time from stimulus to oAP response.
(K) Incidence of the Wenckebach phenomenon in eAVNTs and eVTs.
(L) Assessment for decremental conduction in eAVNTs and eVTs. Change in latency at increasing premature stimulus frequency (S2) (left). S2 frequency at which capture is lost (middle). Slope of the latency increase (right).
(M) Immunofluorescent staining of MSX2 and cTNT. Scale bars, 250 μm. Error bars represent SEM. n = 2–3 from four independent differentiations each. Unpaired t test (D [left], F, and L [middle]); Mann-Whitney test (D [right], I, and L [right]): ***$p < 0.001$.
See also Figure S6.

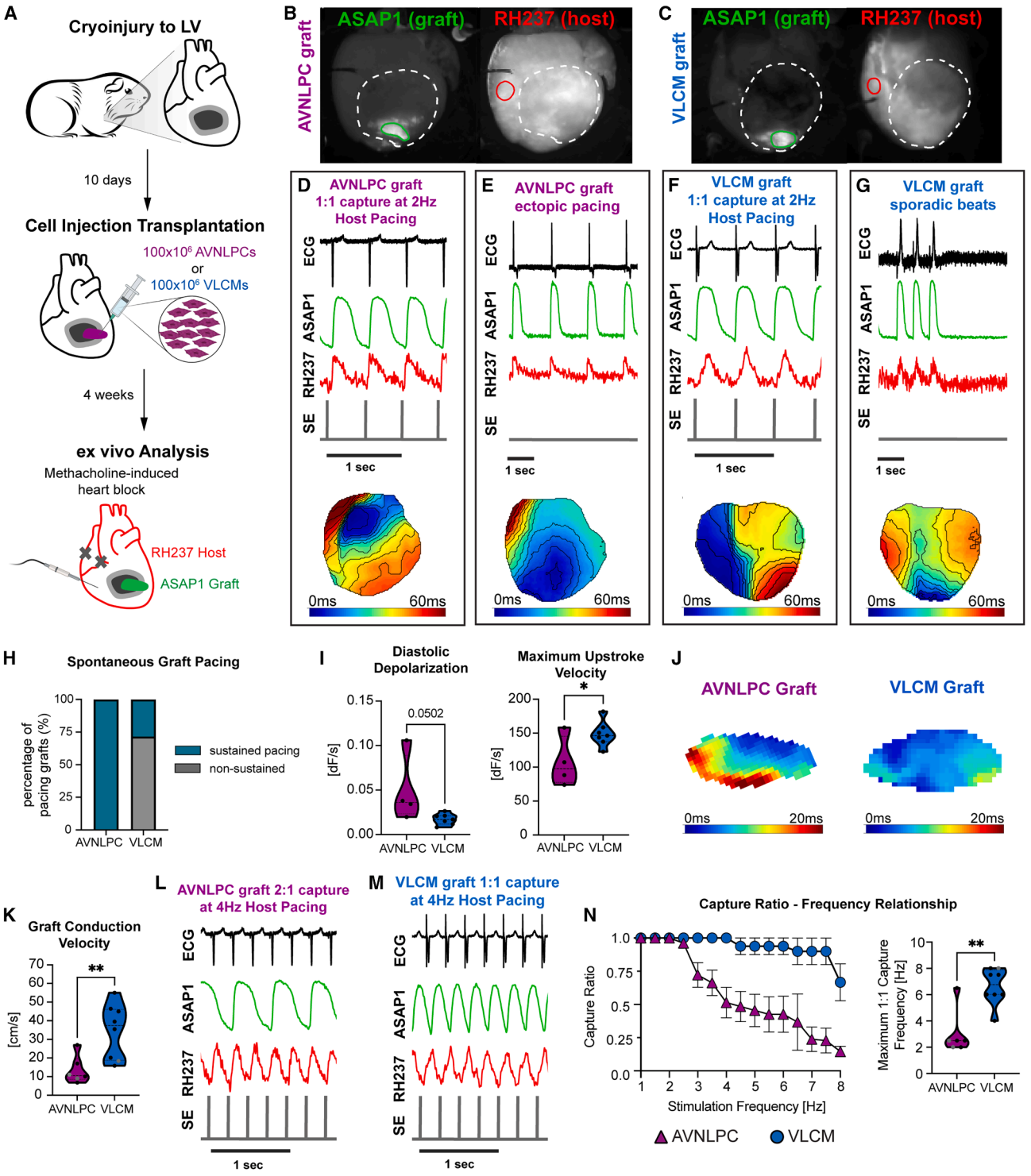

Figure 7. AVNLPCs exhibit AVN conduction properties *in vivo*

(A) Guinea pig cryoinjury model.

(B and C) Hearts containing an ASAP1-derived (B) AVNLPC or (C) VLCM graft acquired in the ASAP1 (green) and RH237 (red) channels. Dotted lines outline the scar. oAPs of the AVNLPC/VLCM grafts and host recorded in the region of interest (ROI) marked in green and red, respectively.

(D–G) Host ECG traces together with oAPs of an (D and E) AVNLPC or (F and G) VLCM graft and the host and the stimulation electrode (SE) signal (D and F) at 2 Hz pacing, and (E and G) without external pacing, in methacholine perfused hearts. Voltage activation maps indicating the origin of pacing (bottom).

(H) Proportion of AVNLPC/VLCM grafts (n = 4/7) showing sustained pacing.

(I) Quantification of oAP parameters in AVNLPC/VLCM grafts (n = 4/7).

(legend continued on next page)

We next leveraged the graft-host coupling to pace the ventricle and assess the conduction properties of the grafts. Grafts that were not coupled were directly paced with the electrode. When we paced the hearts/grafts at 2 Hz, AVNLPC grafts displayed conduction velocities similar to the human AVN (13.5 ± 3.0 cm/s),[1,79,80] significantly slower than VLCM grafts (34.5 ± 5.2 cm/s) (Figures 7J and 7K). To assess whether AVNLPC grafts can block conduction of rapid rhythms, we paced the hearts/grafts at increasing frequencies (Figures 7L–7N). AVNLPC grafts sustained 1:1 capture up to 3.0 ± 0.7 Hz, while VLCM grafts maintained 1:1 capture up to 6.6 ± 0.5 Hz. Finally, hearts were sectioned and stained for human KU80 to identify the grafts (Figures S7F and S7G). AVNLPC grafts stained cTNT^{+}MSX2^{+} while VLCM grafts stained cTNT^{+}MSX2^{low}, confirming graft identity. Together, these experiments show that AVNLPCs can function as a biological pacemaker and maintain AVN conduction properties *in vivo*.

DISCUSSION

Although protocols for AVNLPC differentiation have been described,[39–42] a comprehensive functional evaluation determining their potential for BioCB applications is still lacking. Here, we report an efficient BMP signaling-based approach for generating AVNLPCs from multiple hPSC lines. We show that these AVNLPCs transcriptionally and functionally mimic AVN pacemaker cells. Importantly, AVNLPCs recapitulate the AVN's crucial safety function of blocking fast rates both *in vitro* and *in vivo*. These findings establish a foundation for modeling AVN diseases and the development of a BioCB as a potential treatment for patients with AV block.

We demonstrate that Wnt activation using CHIR99021 induces differentiation of cardiac progenitors toward AVNLPCs. In agreement with developmental literature, this effect is mediated by BMP signaling.[2,30–32] Accordingly, BMP2 is equally potent in inducing AVNLPC differentiation. Of note, using multiple hPSC lines, we found that CHIR99021 but not BMP2 reduced the cardiomyocyte content and that the BMP2-AVNLPC protocol is more robust.

Interestingly, we found a baseline level of NKX2-5^{+}TBX3^{+} pacemaker cells, using standard VLCM differentiation protocols, which is an issue for cell therapies targeting myocardial infarction.[81,82] We show that BMP inhibition at the cardiac progenitor stage removes these pacemaker cells and could therefore enhance the safety of VLCM-based cell therapies.

The AVN is a heterogeneous structure consisting of a core AVN that is surrounded by transitional cell types, including ATZ cells toward the right atrium and LNB cells toward the right ventricle and His bundle.[5,59,79,83–85] Our snRNA-seq analysis of the fetal AVN captured this heterogeneity. Importantly, the AVNLPC cultures similarly contain core AVN, ATZ, and LNB cells. This is the first time that these AVN cardiomyocyte subtypes have been generated from hPSCs, and it underscores the strength of our developmental biology-based approach in capturing native AVN features. Data integration, gene signature scoring, and Spearman correlation analysis using our own and published reference datasets[54,55] confirmed the close resemblance of the AVNLPCs to fetal and adult AVN cells. Heterogeneous AVNLPC cultures might be advantageous for BioCB applications, with transitional cell types facilitating electrical integration with the host and core AVN cells establishing the slow, decremental conduction.

Four other studies reported the generation of AVC/AVN-like cardiomyocytes.[39–42] Using the published scRNA-seq datasets allowed us to show that our AVNLPCs are most similar to the cells generated by Li et al. and Schmidt et al.[42] Of note, our AVNLPCs correlated most closely to fetal and adult AVN samples, suggesting that they might represent a more advanced developmental stage. Use of the HES3 NKX2-5$^{eGFP/wt}$TBX3$^{tdTomato/wt}$ reporter line and MSX2 staining allowed us to determine differentiation efficiencies of 60%–70% for multiple hPSC lines. In contrast, previous studies either lacked quantification across multiple cell lines or reported lower differentiation efficiencies.[39–42]

Both first heart field (FHF) and posterior second heart field (pSHF) contribute to AVC development, but their contribution to the definitive AVN is unresolved.[86–89] Our differentiation transitions through a RALDH2^{-}CD235^{+} mesoderm and addition of RA reduced the AVNLPC population, suggesting a FHF origin.[26,90] Other protocols activate RA signaling using RA or retinol-containing media, suggesting a pSHF origin.[39–42] Notably, these AVC/AVN-like cardiomyocytes highly expressed the fast-conducting Cx40 (*GJA5*), usually expressed by pSHF-derived ALCMs.[40,42] In contrast, our AVNLPCs exhibit low *GJA5* expression, aligning with an AVN phenotype. Future studies should investigate the differences between FHF and pSHF-derived AVC/AVN-like cardiomyocytes and the implications for disease modeling and cell therapies.

Determining whether AVNLPCs resemble AVN or earlier AVC cardiomyocytes is complicated by the lack of definitive markers. In the mouse, the AVN is established by E17,[38,91] corresponding to gestation week 10 of human development.[92–94] Accordingly, the core AVN cluster identified in our gestation week 19 sample represents AVN cardiomyocytes. Spearman correlation analysis demonstrated high similarity between AVNLPCs with this fetal AVN cluster and adult AVN cells, suggesting an AVN phenotype. Besides differentiating into AVN cardiomyocytes, AVC cardiomyocytes differentiate into ALCMs and VLCMs.[34,35] Our *in vivo* experiments demonstrated that AVNLPCs maintain a stable AVN-like phenotype (MSX2 expression and functional properties) for up to 4 weeks. Based on these findings, we refer to our cells as AVNLPCs.

To investigate their conduction properties, we integrated AVNLPCs into EHTs (eAVNTs). eAVNTs exhibited conduction velocities of ~4 cm/s, comparable to the human AVN.[1,79,80] In contrast, eVTs containing VLCMs showed significantly faster conduction velocities. However, conduction remained slower

(J) Graft voltage activation maps.
(K) Conduction velocities recorded in AVNLPC/VLCM grafts (n = 6/8). Gray dots: grafts that were not electrically coupled.
(L and M) Host ECG traces together with oAPs of an (L) AVNLPC or (M) VLCM graft and the host and the SE signal at 4 Hz pacing.
(N) Capture ratios of AVNLPC/VLCM grafts (n = 6/8) at increasing pacing frequencies (left). Frequency at which 1:1 capture is lost (right). Error bars represent SEM. Unpaired t test (I and K); Mann-Whitney test (N): $^{*}p < 0.05$, $^{**}p < 0.01$.
See also Figure S7.

than in native ventricles, most likely due to the immature state of hPSC-derived cardiomyocytes.[95–99]

When eAVNTs were paced rapidly, simulating atrial fibrillation, they blocked conduction of impulses above 3.2 Hz. Analysis of the underlying mechanism revealed that eAVNTs display the Wenckebach phenomenon and decremental conduction. The replication of these complex AVN properties goes beyond previous reports only describing slow conduction velocities[39–42] and provides strong evidence that we generated *bona fide* AVN cells. Notably, eVTs lacked these AVN conduction properties and did not block fast rates effectively. This underscores the importance of generating the correct cardiomyocyte subtype for therapeutic application as a BioCB.

For BioCB applications, it will be important that AVNLPCs maintain their phenotype *in vivo*. Here, we used state-of-the-art voltage sensors and dyes to assess graft-host electrical integration and conduction. We show that AVNLPCs are electrically coupled and, upon pharmacological SAN/AVN block, function as a backup pacemaker, like the genuine AVN. Furthermore, AVNLPCs maintained their conduction properties for 4 weeks post-transplantation, marking a key advancement over *in vitro* studies.[39–42] Although AVNLPC conduction velocity *in vivo* was faster than *in vitro* (13.5 ± 3.0 vs. 3.8 ± 0.4 cm/s), likely reflecting graft maturation, it remained within the range of the human AVN.[1,79,80] Importantly, AVNLPCs maintained the ability to block fast pacing rates above 3.0 Hz, in contrast to VLCMs that only blocked rates above 6.6 Hz. Conduction of rates >6 Hz (360 bpm) to the ventricles would be life threatening in humans, again underscoring the importance of generating the appropriate cell type for the therapeutic application in question—in this case, AVNLPCs, and not VLCMs, for safe and effective future BioCB therapies.

Limitations of the study

AVNLPC cultures contain a mix of core AVN, ATZ, and LNB cells. Future studies will focus on identifying the signaling pathways that specifically drive the differentiation of each of these subtypes and their relevance for BioCB applications. We would also like to acknowledge that we did not fully determine the ability of AVNLPCs to function as a BioCB between the atria and ventricles. This was challenging using small animal models, and attempts to suture the eAVNTs into the AV groove failed due to the lack of electrical integration with the host hearts. Future studies in large animal AV block models, such as the pig, which allow for better surgical manipulation of the heart and delivery of AVNLPCs into the AVN region, will be required. These studies will be essential to assess the function, durability, and potential arrhythmogenic risks of an AVNLPC-based BioCB. Finally, like every hPSC-derived product, AVNLPCs are immature and do not represent adult AVN cells. However, we were able to show striking functional differences between AVNLPCs and VLCMs, demonstrating that these cells are a valuable tool for *in vitro* AVN disease modeling and the development of a BioCB for patients with AV block.

RESOURCE AVAILABILITY

Lead contact

Requests for resources and reagents should be directed to the lead contact, Stephanie Protze (stephanie.protze@uhn.ca).

Materials availability

The HES3-Nkx2-5$^{egfp/wt}$TBX3$^{tdtomato/wt}$ hPSCs are available from the lead contact with a completed material transfer agreement.

Data and code availability

- sc/snRNA-seq data generated in this study have been deposited in the GEO database under GEO: GSE297072 and GEO: GSE297073 and are publicly available as of the date of publication.
- This paper analyzes existing, publicly available data. The accession numbers for these datasets are in the key resources table.
- This paper does not report original code.
- Any additional information required to reanalyze the data reported in this paper is available from the lead contact upon request.

ACKNOWLEDGMENTS

We would like to thank all Protze laboratory members for advice on the manuscript. We thank Professors A. Elefanty and E. Stanley (Monash University, Victoria, AU) for providing the NKX2-5$^{egfp/wt}$ hPSCs. We thank Dr. F. Alibhai (UHN, Toronto, CA) for feedback on the optical mapping analysis. We also like to thank the following core facilities: SickKids-UHN Flow Cytometry Facility, SickKids Imaging Facility, UHN Advanced Optical Microscopy Facility, Princess Margaret Genomics Centre, and UHN Animal Resource Centre. We thank the donors, the Research Centre for Women's and Infants' Health BioBank Program, the Lunenfeld-Tannenbaum Research Institute, and the Department of Obstetrics & Gynecology of Sinai Health System for the human specimens used in this study. This work was supported by grants from the Canadian Institutes of Health Research (CIHR) (PJT-169090, S.P.), Canadian Stem Cell Network (ECR-C5R1-9, S.P.), Canadian Foundation for Innovation (38651, S.P.), Government of Canada's New Frontiers in Research Fund (NRFT-2022-00447, M.A.L.), Canada Research Chairs Program (CRC-2020-00245, M.A.L.), and funding from BlueRock Therapeutics LP (S.P.). M.L. was supported by a CIHR Masters Fellowship. M.L., A.A.L., and A.L.Y.X. were supported by Ontario Graduate Scholarships; B.M.M. and M.L.C. were supported by CIHR Doctoral Fellowships. Adobe Illustrator was used to prepare figures. Biorender was used to generate schematics.

AUTHOR CONTRIBUTIONS

M.L. designed the project, performed experiments, analyzed data, and wrote the manuscript. M.L., M.K., R.S., and M.C. performed and analyzed tissue culture and flow cytometry experiments. O. Mourad, O. Mastikhina, K.S., and S.S.N. designed and generated the EHTs. S.P. performed and analyzed the patch clamp experiments. M.L., S.P., S.M., and K.N. designed, performed and analyzed the optical mapping experiments of the EHTs. M.L., B.M.M., S.P., W.D., and M.A.L. designed, performed, and analyzed the optical mapping experiments of the guinea pig hearts. A.L.Y.X. assisted with analysis of optical mapping data. M.E. and B.Q. assisted with guinea pig surgeries and cell injections. M.L.C. assisted with immunohistochemistry experiments and imaging. S.K. designed and generated the NKX2-5$^{eGFP/wt}$ TBX3$^{tdTomato/wt}$ hPSCs. A.M. assisted with the dissection of fetal heart tissues. A.A.L., M.L., and S.P. generated and analyzed the sc/snRNA-seq data. S.P. designed the project and wrote the manuscript.

DECLARATION OF INTERESTS

M.A.L. is a scientific founder and consultant for BlueRock Therapeutics LP. M.L. and S.P. declare a patent (PCT/CA2023/050936) related to this study.

STAR★METHODS

Detailed methods are provided in the online version of this paper and include the following:

- KEY RESOURCES TABLE
- EXPERIMENTAL MODEL AND STUDY PARTICIPANT DETAILS
  - Human ESC lines

SUPPLEMENTAL INFORMATION

Supplemental information can be found online at https://doi.org/10.1016/j.stem.2026.02.012.

Received: June 27, 2025
Revised: January 4, 2026
Accepted: February 27, 2026
Published: March 23, 2026

REFERENCES

1. Katz, A.M. (2013). Physiology of the Heart, Fifth Edition (Lippincott Williams & Wilkins (LWW)).
2. Christoffels, V.M., Smits, G.J., Kispert, A., and Moorman, A.F.M. (2010). Development of the Pacemaker Tissues of the Heart. Circ. Res. *106*, 240–254. https://doi.org/10.1161/CIRCRESAHA.109.205419.
3. Buijtendijk, M.F.J., Barnett, P., and Van Den Hoff, M.J.B. (2020). Development of the human heart. Am. J. Med. Genet., C *184*, 7–22. https://doi.org/10.1002/ajmg.c.31778.
4. Mazgalev, T., Vann Wagoner, D., and Efimov, I.R. (2004). Mechanisms of Atrioventricular Nodal Excitability and Propagation. https://clinicalgate.com/mechanisms-of-atrioventricular-nodal-excitability-and-propagation/.
5. Kurian, T., Ambrosi, C., Hucker, W., Fedorov, V.V., and Efimov, I.R. (2010). Anatomy and Electrophysiology of the Human AV Node. Pacing Clin. Electrophysiol. *33*, 754–762. https://doi.org/10.1111/j.1540-8159.2010.02699.x.
6. Choi, B.-R., Ziv, O., and Salama, G. (2023). Conduction delays across the specialized conduction system of the heart: Revisiting atrioventricular node (AVN) and Purkinje-ventricular junction (PVJ) delays. Front. Cardiovasc. Med. *10*, 1158480. https://doi.org/10.3389/fcvm.2023.1158480.
7. Ferrier, G.R., and Dresel, P.E. (1974). Relationship of the Functional Refractory Period to Conduction in the Atrioventricular Node. Circ. Res. *35*, 204–214. https://doi.org/10.1161/01.RES.35.2.204.
8. Levy, M.N., Martin, P.J., Edelstein, J., and Goldberg, L.B. (1974). The AV nodal Wenckebach phenomenon as a positive feedback mechanism. Prog. Cardiovasc. Dis. *16*, 601–613. https://doi.org/10.1016/0033-0620(74)90020-6.
9. Hoshino, K., Anumonwo, J., Delmar, M., and Jalife, J. (1990). Wenckebach periodicity in single atrioventricular nodal cells from the rabbit heart. Circulation *82*, 2201–2216. https://doi.org/10.1161/01.CIR.82.6.2201.
10. Billette, J., and Nattel, S. (1994). Dynamic Behavior of the Atrioventricular Node: A Functional Model of Interaction Between Recovery, Facilitation, and Fatigue. J. Cardiovasc. Electrophysiol. *5*, 90–102. https://doi.org/10.1111/j.1540-8167.1994.tb01117.x.
11. Mendenhall, G.S., Voigt, A., and Saba, S. (2013). Insights Into Atrioventricular Nodal Function From Patients Displaying Dual Conduction Properties: Interactive and Orthogonal Pathways. Circ. Arrhythm. Electrophysiol. *6*, 364–370. https://doi.org/10.1161/CIRCEP.113.000248.
12. Boriani, G., and Raatikainen, M.J.P. (2018). Anatomy and physiology of the atrioventricular node. In The ESC Textbook of Cardiovascular Medicine He European Society of Cardiology Series (ESC Publications), pp. 1958–1959.
13. Boyett, M.R., Honjo, H., and Kodama, I. (2000). The sinoatrial node, a heterogeneous pacemaker structure. Cardiovasc. Res. *47*, 658–687. https://doi.org/10.1016/S0008-6363(00)00135-8.
14. Vassalle, M. (1977). The relationship among cardiac pacemakers. Overdrive suppression. Circ. Res. *41*, 269–277. https://doi.org/10.1161/01.RES.41.3.269.
15. Wood, M.A., and Ellenbogen, K.A. (2002). Cardiology Patient Pages. Cardiac Pacemakers From the Patient's Perspective. Circulation *105*, 2136–2138. https://doi.org/10.1161/01.CIR.0000016183.07898.90.
16. Mond, H.G., and Proclemer, A. (2011). The 11th world survey of cardiac pacing and implantable cardioverter-defibrillators: calendar year 2009–a World Society of Arrhythmia's project. Pacing Clin. Electrophysiol. *34*, 1013–1027. https://doi.org/10.1111/j.1540-8159.2011.03150.x.
17. Cantillon, D.J., Exner, D.V., Badie, N., Davis, K., Gu, N.Y., Nabutovsky, Y., and Doshi, R. (2017). Complications and Health Care Costs Associated With Transvenous Cardiac Pacemakers in a Nationwide Assessment. JACC Clin. Electrophysiol. *3*, 1296–1305. https://doi.org/10.1016/j.jacep.2017.05.007.
18. Kirkfeldt, R.E., Johansen, J.B., Nohr, E.A., Jørgensen, O.D., and Nielsen, J.C. (2014). Complications after cardiac implantable electronic device implantations: an analysis of a complete, nationwide cohort in Denmark. Eur. Heart J. *35*, 1186–1194. https://doi.org/10.1093/eurheartj/eht511.
19. Udo, E.O., Zuithoff, N.P.A., Van Hemel, N.M., De Cock, C.C., Hendriks, T., Doevendans, P.A., and Moons, K.G.M. (2012). Incidence and predictors of short- and long-term complications in pacemaker therapy: The FOLLOWPACE study. Heart Rhythm *9*, 728–735. https://doi.org/10.1016/j.hrthm.2011.12.014.
20. Sanderson, J.E., and Yu, C.-M. (2012). Can cardiac resynchronization therapy cause harm? Eur. Heart J. *33*, 816–818. https://doi.org/10.1093/eurheartj/ehr478.
21. Vatankulu, M.A., Goktekin, O., Kaya, M.G., Ayhan, S., Kucukdurmaz, Z., Sutton, R., and Henein, M. (2009). Effect of Long-Term Resynchronization Therapy on Left Ventricular Remodeling in Pacemaker Patients Upgraded to Biventricular Devices. Am. J. Cardiol. *103*, 1280–1284. https://doi.org/10.1016/j.amjcard.2009.01.023.
22. Eliasson, H., Sonesson, S.-E., Salomonsson, S., Skog Andreasson, A., Wahren-Herlenius, M., and Gadler, F. (2019). Pacing therapy in children with isolated complete atrioventricular block: a retrospective study of pacing system survival and pacing-related complications in a national cohort. Europace *21*, 1717–1724. https://doi.org/10.1093/europace/euz268.
23. Lian, X., Hsiao, C., Wilson, G., Zhu, K., Hazeltine, L.B., Azarin, S.M., Raval, K.K., Zhang, J., Kamp, T.J., and Palecek, S.P. (2012). Robust cardiomyocyte differentiation from human pluripotent stem cells via temporal modulation of canonical Wnt signaling. Proc. Natl. Acad. Sci. USA *109*, E1848–E1857. https://doi.org/10.1073/pnas.1200250109.
24. Burridge, P.W., Matsa, E., Shukla, P., Lin, Z.C., Churko, J.M., Ebert, A.D., Lan, F., Diecke, S., Huber, B., Mordwinkin, N.M., et al. (2014). Chemically defined generation of human cardiomyocytes. Nat. Methods *11*, 855–860. https://doi.org/10.1038/nmeth.2999.
25. Devalla, H.D., Schwach, V., Ford, J.W., Milnes, J.T., El-Haou, S., Jackson, C., Gkatzis, K., Elliott, D.A., Chuva De Sousa Lopes, S.M., Mummery, C.L., et al. (2015). Atrial-like cardiomyocytes from human pluripotent stem cells are a robust preclinical model for assessing atrial-selective pharmacology. EMBO Mol. Med. *7*, 394–410. https://doi.org/10.15252/emmm.201404757.
26. Lee, J.H., Protze, S.I., Laksman, Z., Backx, P.H., and Keller, G.M. (2017). Human Pluripotent Stem Cell-Derived Atrial and Ventricular

Cardiomyocytes Develop from Distinct Mesoderm Populations. Cell Stem Cell *21*, 179–194.e4. https://doi.org/10.1016/j.stem.2017.07.003.

27. Birket, M.J., Ribeiro, M.C., Verkerk, A.O., Ward, D., Leitoguinho, A.R., Den Hartogh, S.C., Orlova, V.V., Devalla, H.D., Schwach, V., Bellin, M., et al. (2015). Expansion and patterning of cardiovascular progenitors derived from human pluripotent stem cells. Nat. Biotechnol. *33*, 970–979. https://doi.org/10.1038/nbt.3271.
28. Protze, S.I., Liu, J., Nussinovitch, U., Ohana, L., Backx, P.H., Gepstein, L., and Keller, G.M. (2017). Sinoatrial node cardiomyocytes derived from human pluripotent cells function as a biological pacemaker. Nat. Biotechnol. *35*, 56–68. https://doi.org/10.1038/nbt.3745.
29. Protze, S.I., Lee, J.H., and Keller, G.M. (2019). Human Pluripotent Stem Cell-Derived Cardiovascular Cells: From Developmental Biology to Therapeutic Applications. Cell Stem Cell *25*, 311–327. https://doi.org/10.1016/j.stem.2019.07.010.
30. Verhoeven, M.C., Haase, C., Christoffels, V.M., Weidinger, G., and Bakkers, J. (2011). Wnt signaling regulates atrioventricular canal formation upstream of *BMP* and *Tbx2*. Birth Defects Res. A Clin. Mol. Teratol. *91*, 435–440. https://doi.org/10.1002/bdra.20804.
31. Gillers, B.S., Chiplunkar, A., Aly, H., Valenta, T., Basler, K., Christoffels, V.M., Efimov, I.R., Boukens, B.J., and Rentschler, S. (2015). Canonical Wnt Signaling Regulates Atrioventricular Junction Programming and Electrophysiological Properties. Circ. Res. *116*, 398–406. https://doi.org/10.1161/CIRCRESAHA.116.304731.
32. Yamada, M., Revelli, J.P., Eichele, G., Barron, M., and Schwartz, R.J. (2000). Expression of Chick Tbx-2, Tbx-3, and Tbx-5 Genes during Early Heart Development: Evidence for BMP2 Induction of Tbx2. Dev. Biol. *228*, 95–105. https://doi.org/10.1006/dbio.2000.9927.
33. Van Eif, V.W.W., Devalla, H.D., Boink, G.J.J., and Christoffels, V.M. (2018). Transcriptional regulation of the cardiac conduction system. Nat. Rev. Cardiol. *15*, 617–630. https://doi.org/10.1038/s41569-018-0031-y.
34. Aanhaanen, W.T.J., Brons, J.F., Domínguez, J.N., Rana, M.S., Norden, J., Airik, R., Wakker, V., De Gier-de Vries, C., Brown, N.A., Kispert, A., et al. (2009). The *Tbx2*+ primary myocardium of the atrioventricular canal forms the atrioventricular node and the base of the left ventricle. Circ. Res. *104*, 1267–1274. https://doi.org/10.1161/CIRCRESAHA.108.192450.
35. Kim, J.S., Virágh, S., Moorman, A.F.M., Anderson, R.H., and Lamers, W.H. (2001). Development of the Myocardium of the Atrioventricular Canal and the Vestibular Spine in the Human Heart. Circ. Res. *88*, 395–402. https://doi.org/10.1161/01.RES.88.4.395.
36. Christoffels, V.M., Mommersteeg, M.T.M., Trowe, M.-O., Prall, O.W.J., De Gier-de Vries, C., Soufan, A.T., Bussen, M., Schuster-Gossler, K., Harvey, R.P., Moorman, A.F.M., et al. (2006). Formation of the Venous Pole of the Heart From an *Nkx2–5* –Negative Precursor Population Requires *Tbx18*. Circ. Res. *98*, 1555–1563. https://doi.org/10.1161/01.RES.0000227571.84189.65.
37. Christoffels, V.M., and Moorman, A.F.M. (2009). Development of the Cardiac Conduction System: Why Are Some Regions of the Heart More Arrhythmogenic Than Others? Circ. Arrhythm. Electrophysiol. *2*, 195–207. https://doi.org/10.1161/CIRCEP.108.829341.
38. Goodyer, W.R., Beyersdorf, B.M., Paik, D.T., Tian, L., Li, G., Buikema, J.W., Chirikian, O., Choi, S., Venkatraman, S., Adams, E.L., et al. (2019). Transcriptomic Profiling of the Developing Cardiac Conduction System at Single-Cell Resolution. Circ. Res. *125*, 379–397. https://doi.org/10.1161/CIRCRESAHA.118.314578.
39. Du, R., Bai, S., Zhao, Y., and Ma, Y. (2023). Efficient generation of TBX3+ atrioventricular conduction-like cardiomyocytes from human pluripotent stem cells. Biochem. Biophys. Res. Commun. *669*, 143–149. https://doi.org/10.1016/j.bbrc.2023.05.104.
40. Ye, C., Yang, C., Zhang, H., Gao, R., Liao, Y., Zhang, Y., Jie, L., Zhang, Y., Cheng, T., Wang, Y., et al. (2024). Canonical Wnt signaling directs the generation of functional human PSC-derived atrioventricular canal cardiomyocytes in bioprinted cardiac tissues. Cell Stem Cell *31*, 398–409.e5. https://doi.org/10.1016/j.stem.2024.01.008.
41. Li, J., Wiesinger, A., Fokkert, L., Bakker, P., De Vries, D.K., Tijsen, A.J., Pinto, Y.M., Verkerk, A.O., Christoffels, V.M., Boink, G.J.J., et al. (2024). Modeling the atrioventricular conduction axis using human pluripotent stem cell-derived cardiac assembloids. Cell Stem Cell *31*, 1667–1684.e6. https://doi.org/10.1016/j.stem.2024.08.008.
42. Schmidt, C., Deyett, A., Ilmer, T., Haendeler, S., Torres Caballero, A., Novatchkova, M., Netzer, M.A., Ceci Ginistrelli, L., Mancheno Juncosa, E., Bhattacharya, T., et al. (2023). Multi-chamber cardioids unravel human heart development and cardiac defects. Cell *186*, 5587–5605.e27. https://doi.org/10.1016/j.cell.2023.10.030.
43. Elliott, D.A., Braam, S.R., Koutsis, K., Ng, E.S., Jenny, R., Lagerqvist, E.L., Biben, C., Hatzistavrou, T., Hirst, C.E., Yu, Q.C., et al. (2011). NKX2-5eGFP/w hESCs for isolation of human cardiac progenitors and cardiomyocytes. Nat. Methods *8*, 1037–1040. https://doi.org/10.1038/nmeth.1740.
44. Dubois, N.C., Craft, A.M., Sharma, P., Elliott, D.A., Stanley, E.G., Elefanty, A.G., Gramolini, A., and Keller, G. (2011). SIRPA is a specific cell-surface marker for isolating cardiomyocytes derived from human pluripotent stem cells. Nat. Biotechnol. *29*, 1011–1018. https://doi.org/10.1038/nbt.2005.
45. Bakker, M.L., Moorman, A.F.M., and Christoffels, V.M. (2010). The Atrioventricular Node: Origin, Development, and Genetic Program. Trends Cardiovasc. Med. *20*, 164–171. https://doi.org/10.1016/j.tcm.2011.02.001.
46. Hafeez, Y., and Grossman, S., A. (2023). Junctional Rhythm. StatPearls. https://www.ncbi.nlm.nih.gov/books/NBK507715/.
47. DiFrancesco, D. (1993). Pacemaker Mechanisms in Cardiac Tissue. Annu. Rev. Physiol. *55*, 455–472. https://doi.org/10.1146/annurev.ph.55.030193.002323.
48. He, J.-Q., Ma, Y., Lee, Y., Thomson, J.A., and Kamp, T.J. (2003). Human Embryonic Stem Cells Develop Into Multiple Types of Cardiac Myocytes: Action Potential Characterization. Circ. Res. *93*, 32–39. https://doi.org/10.1161/01.RES.0000080317.92718.99.
49. Rentschler, S., Harris, B.S., Kuznekoff, L., Jain, R., Manderfield, L., Lu, M.M., Morley, G.E., Patel, V.V., and Epstein, J.A. (2011). Notch signaling regulates murine atrioventricular conduction and the formation of accessory pathways. J. Clin. Investig. *121*, 525–533. https://doi.org/10.1172/JCI44470.
50. Rutenberg, J.B., Fischer, A., Jia, H., Gessler, M., Zhong, T.P., and Mercola, M. (2006). Developmental patterning of the cardiac atrioventricular canal by Notch and Hairy-related transcription factors. Development *133*, 4381–4390. https://doi.org/10.1242/dev.02607.
51. Dhahri, W., Sadikov Valdman, T., Wilkinson, D., Pereira, E., Ceylan, E., Andharia, N., Qiang, B., Masoudpour, H., Wulkan, F., Quesnel, E., et al. (2022). In Vitro Matured Human Pluripotent Stem Cell–Derived Cardiomyocytes Form Grafts With Enhanced Structure and Function in Injured Hearts. Circulation *145*, 1412–1426. https://doi.org/10.1161/CIRCULATIONAHA.121.053563.
52. Reubinoff, B.E., Pera, M.F., Fong, C.Y., Trounson, A., and Bongso, A. (2000). Embryonic stem cell lines from human blastocysts: somatic differentiation in vitro. Nat. Biotechnol. *18*, 399–404. https://doi.org/10.1038/74447.
53. Lim, A.A., Pouyabahar, D., Ashraf, M., Huang, K., Lohbihler, M., Murareanu, B.M., Chang, M.L., Kwan, M., Alibhai, F.J., Tran, T., et al. (2024). Single-cell transcriptome analysis reveals CD34 as a marker of human sinoatrial node pacemaker cardiomyocytes. Nat. Commun. *15*, 10206. https://doi.org/10.1038/s41467-024-54337-4.
54. Farah, E.N., Hu, R.K., Kern, C., Zhang, Q., Lu, T.-Y., Ma, Q., Tran, S., Zhang, B., Carlin, D., Monell, A., et al. (2024). Spatially organized cellular communities form the developing human heart. Nature *627*, 854–864. https://doi.org/10.1038/s41586-024-07171-z.
55. Kanemaru, K., Cranley, J., Muraro, D., Miranda, A.M.A., Ho, S.Y., Wilbrey-Clark, A., Patrick Pett, J., Polanski, K., Richardson, L., Litvinukova, M., et al. (2023). Spatially resolved multiomics of human cardiac niches. Nature *619*, 801–810. https://doi.org/10.1038/s41586-023-06311-1.

56. Aibar, S., González-Blas, C.B., Moerman, T., Huynh-Thu, V.A., Imrichova, H., Hulselmans, G., Rambow, F., Marine, J.-C., Geurts, P., Aerts, J., et al. (2017). SCENIC: single-cell regulatory network inference and clustering. Nat. Methods *14*, 1083–1086. https://doi.org/10.1038/nmeth.4463.

57. Van De Sande, B., Flerin, C., Davie, K., De Waegeneer, M., Hulselmans, G., Aibar, S., Seurinck, R., Saelens, W., Cannoodt, R., Rouchon, Q., et al. (2020). A scalable SCENIC workflow for single-cell gene regulatory network analysis. Nat. Protoc. *15*, 2247–2276. https://doi.org/10.1038/s41596-020-0336-2.

58. Hoogaars, W.M.H., Engel, A., Brons, J.F., Verkerk, A.O., De Lange, F.J., Wong, L.Y.E., Bakker, M.L., Clout, D.E., Wakker, V., Barnett, P., et al. (2007). Tbx3 controls the sinoatrial node gene program and imposes pacemaker function on the atria. Genes Dev. *21*, 1098–1112. https://doi.org/10.1101/gad.416007.

59. Oh, Y., Abid, R., Dababneh, S., Bakr, M., Aslani, T., Cook, D.P., Vanderhyden, B.C., Park, J.G., Munshi, N.V., Hui, C.-C., et al. (2024). Transcriptional regulation of the postnatal cardiac conduction system heterogeneity. Nat. Commun. *15*, 6550. https://doi.org/10.1038/s41467-024-50849-1.

60. Bakr, M. (2025). Conservation and divergence of transcriptional heterogeneity in the cardiac conduction system. Preprint at bioRxiv. https://doi.org/10.1101/2025.09.23.678069.

61. Cai, B., Wang, N., Mao, W., You, T., Lu, Y., Li, X., Ye, B., Li, F., and Xu, H. (2014). Deletion of FoxO1 leads to shortening of QRS by increasing Na+ channel activity through enhanced expression of both cardiac NaV1.5 and β3 subunit. J. Mol. Cell. Cardiol. *74*, 297–306. https://doi.org/10.1016/j.yjmcc.2014.06.006.

62. Aanhaanen, W.T.J., Boukens, B.J.D., Sizarov, A., Wakker, V., De Gier-de Vries, C., Van Ginneken, A.C., Moorman, A.F.M., Coronel, R., and Christoffels, V.M. (2011). Defective Tbx2-dependent patterning of the atrioventricular canal myocardium causes accessory pathway formation in mice. J. Clin. Investig. *121*, 534–544. https://doi.org/10.1172/JCI44350.

63. Ahuja, S., Dogra, D., Stainier, D.Y.R., and Reischauer, S. (2016). Id4 functions downstream of Bmp signaling to restrict TCF function in endocardial cells during atrioventricular valve development. Dev. Biol. *412*, 71–82. https://doi.org/10.1016/j.ydbio.2016.02.003.

64. Chamberland, S., Yang, H.H., Pan, M.M., Evans, S.W., Guan, S., Chavarha, M., Yang, Y., Salesse, C., Wu, H., Wu, J.C., et al. (2017). Fast two-photon imaging of subcellular voltage dynamics in neuronal tissue with genetically encoded indicators. eLife *6*, e25690. https://doi.org/10.7554/eLife.25690.

65. St-Pierre, F., Marshall, J.D., Yang, Y., Gong, Y., Schnitzer, M.J., and Lin, M.Z. (2014). High-fidelity optical reporting of neuronal electrical activity with an ultrafast fluorescent voltage sensor. Nat. Neurosci. *17*, 884–889. https://doi.org/10.1038/nn.3709.

66. Leyton-Mange, J.S., Mills, R.W., Macri, V.S., Jang, M.Y., Butte, F.N., Ellinor, P.T., and Milan, D.J. (2014). Rapid Cellular Phenotyping of Human Pluripotent Stem Cell-Derived Cardiomyocytes using a Genetically Encoded Fluorescent Voltage Sensor. Stem Cell Rep. *2*, 163–170. https://doi.org/10.1016/j.stemcr.2014.01.003.

67. Mastikhina, O., Moon, B.-U., Williams, K., Hatkar, R., Gustafson, D., Mourad, O., Sun, X., Koo, M., Lam, A.Y.L., Sun, Y., et al. (2020). Human cardiac fibrosis-on-a-chip model recapitulates disease hallmarks and can serve as a platform for drug testing. Biomaterials *233*, 119741. https://doi.org/10.1016/j.biomaterials.2019.119741.

68. Koulouris, S., and Cascella, M. (2023). Electrophysiologic Study Interpretation. StatPearls. https://www.ncbi.nlm.nih.gov/books/NBK560784/.

69. Negru, A.G., and Alzahrani, T. (2023). Electrophysiologic Testing. StatPearls. https://www.ncbi.nlm.nih.gov/books/NBK551499/.

70. Workman, A.J., Kane, K.A., and Rankin, A.C. (2000). Rate-dependency of Action Potential Duration and Refractoriness in Isolated Myocytes from the Rabbit AV Node and Atrium. J. Mol. Cell. Cardiol. *32*, 1525–1537. https://doi.org/10.1006/jmcc.2000.1186.

71. Gerbin, K.A., Yang, X., Murry, C.E., and Coulombe, K.L.K. (2015). Enhanced Electrical Integration of Engineered Human Myocardium via Intramyocardial versus Epicardial Delivery in Infarcted Rat Hearts. PLoS One *10*, e0131446. https://doi.org/10.1371/journal.pone.0131446.

72. Shadrin, I.Y., Allen, B.W., Qian, Y., Jackman, C.P., Carlson, A.L., Juhas, M.E., and Bursac, N. (2017). Cardiopatch platform enables maturation and scale-up of human pluripotent stem cell-derived engineered heart tissues. Nat. Commun. *8*, 1825. https://doi.org/10.1038/s41467-017-01946-x.

73. Jackman, C.P., Ganapathi, A.M., Asfour, H., Qian, Y., Allen, B.W., Li, Y., and Bursac, N. (2018). Engineered cardiac tissue patch maintains structural and electrical properties after epicardial implantation. Biomaterials *159*, 48–58. https://doi.org/10.1016/j.biomaterials.2018.01.002.

74. Jabbour, R.J., Owen, T.J., Pandey, P., Reinsch, M., Wang, B., King, O., Couch, L.S., Pantou, D., Pitcher, D.S., Chowdhury, R.A., et al. (2021). In vivo grafting of large engineered heart tissue patches for cardiac repair. JCI Insight *6*, e144068. https://doi.org/10.1172/jci.insight.144068.

75. Shiba, Y., Fernandes, S., Zhu, W.-Z., Filice, D., Muskheli, V., Kim, J., Palpant, N.J., Gantz, J., Moyes, K.W., Reinecke, H., et al. (2012). Human ES-cell-derived cardiomyocytes electrically couple and suppress arrhythmias in injured hearts. Nature *489*, 322–325. https://doi.org/10.1038/nature11317.

76. Filice, D., Dhahri, W., Solan, J.L., Lampe, P.D., Steele, E., Milani, N., Van Biber, B., Zhu, W.-Z., Valdman, T.S., Romagnuolo, R., et al. (2020). Optical mapping of human embryonic stem cell-derived cardiomyocyte graft electrical activity in injured hearts. Stem Cell Res. Ther. *11*, 417. https://doi.org/10.1186/s13287-020-01919-w.

77. Shiba, Y., Filice, D., Fernandes, S., Minami, E., Dupras, S.K., Biber, B.V., Trinh, P., Hirota, Y., Gold, J.D., Viswanathan, M., et al. (2014). Electrical Integration of Human Embryonic Stem Cell-Derived Cardiomyocytes in a Guinea Pig Chronic Infarct Model. J. Cardiovasc. Pharmacol. Ther. *19*, 368–381. https://doi.org/10.1177/1074248413520344.

78. Mangoni, M.E., and Nargeot, J. (2008). Genesis and Regulation of the Heart Automaticity. Physiol. Rev. *88*, 919–982. https://doi.org/10.1152/physrev.00018.2007.

79. Greener, I.D., Monfredi, O., Inada, S., Chandler, N.J., Tellez, J.O., Atkinson, A., Taube, M.A., Billeter, R., Anderson, R.H., Efimov, I.R., et al. (2011). Molecular architecture of the human specialised atrioventricular conduction axis. J. Mol. Cell. Cardiol. *50*, 642–651. https://doi.org/10.1016/j.yjmcc.2010.12.017.

80. Kupersmith, J., Krongrad, E., and Waldo, A.L. (1973). Conduction Intervals and Conduction Velocity in the Human Cardiac Conduction System: Studies during Open-Heart Surgery. Circulation *47*, 776–785. https://doi.org/10.1161/01.CIR.47.4.776.

81. Romagnuolo, R., Masoudpour, H., Porta-Sánchez, A., Qiang, B., Barry, J., Laskary, A., Qi, X., Massé, S., Magtibay, K., Kawajiri, H., et al. (2019). Human Embryonic Stem Cell-Derived Cardiomyocytes Regenerate the Infarcted Pig Heart but Induce Ventricular Tachyarrhythmias. Stem Cell Rep. *12*, 967–981. https://doi.org/10.1016/j.stemcr.2019.04.005.

82. Liu, Y.-W., Chen, B., Yang, X., Fugate, J.A., Kalucki, F.A., Futakuchi-Tsuchida, A., Couture, L., Vogel, K.W., Astley, C.A., Baldessari, A., et al. (2018). Human embryonic stem cell–derived cardiomyocytes restore function in infarcted hearts of non-human primates. Nat. Biotechnol. *36*, 597–605. https://doi.org/10.1038/nbt.4162.

83. Aanhaanen, W.T.J., Mommersteeg, M.T.M., Norden, J., Wakker, V., De Gier-de Vries, C., Anderson, R.H., Kispert, A., Moorman, A.F.M., and Christoffels, V.M. (2010). Developmental Origin, Growth, and Three-Dimensional Architecture of the Atrioventricular Conduction Axis of the Mouse Heart. Circ. Res. *107*, 728–736. https://doi.org/10.1161/CIRCRESAHA.110.222992.

84. Hucker, W.J., Sharma, V., Nikolski, V.P., and Efimov, I.R. (2007). Atrioventricular conduction with and without AV nodal delay: two pathways to the bundle of His in the rabbit heart. Am. J. Physiol., Heart Circ. Physiol. *293*, H1122–H1130. https://doi.org/10.1152/ajpheart.00115.2007.

85. George, S.A., Faye, N.R., Murillo-Berlioz, A., Lee, K.B., Trachiotis, G.D., and Efimov, I.R. (2017). At the Atrioventricular Crossroads: Dual Pathway Electrophysiology in the Atrioventricular Node and its underlying

Heterogeneities. Arrhythm. Electrophysiol. Rev. *6*, 179–185. https://doi.org/10.15420/aer.2017.30.1.

86. Meilhac, S.M., and Buckingham, M.E. (2018). The deployment of cell lineages that form the mammalian heart. Nat. Rev. Cardiol. *15*, 705–724. https://doi.org/10.1038/s41569-018-0086-9.
87. Meilhac, S.M., Esner, M., Kelly, R.G., Nicolas, J.-F., and Buckingham, M.E. (2004). The Clonal Origin of Myocardial Cells in Different Regions of the Embryonic Mouse Heart. Dev. Cell *6*, 685–698. https://doi.org/10.1016/S1534-5807(04)00133-9.
88. Miquerol, L., Bellon, A., Moreno, N., Beyer, S., Meilhac, S.M., Buckingham, M., Franco, D., and Kelly, R.G. (2013). Resolving cell lineage contributions to the ventricular conduction system with a Cx40-GFP allele: A dual contribution of the first and second heart fields. Dev. Dyn. *242*, 665–677. https://doi.org/10.1002/dvdy.23964.
89. De Soysa, T.Y., Ranade, S.S., Okawa, S., Ravichandran, S., Huang, Y., Salunga, H.T., Schricker, A., Del Sol, A., Gifford, C.A., and Srivastava, D. (2019). Single-cell analysis of cardiogenesis reveals basis for organ-level developmental defects. Nature *572*, 120–124. https://doi.org/10.1038/s41586-019-1414-x.
90. Yang, D., Gomez-Garcia, J., Funakoshi, S., Tran, T., Fernandes, I., Bader, G.D., Laflamme, M.A., and Keller, G.M. (2022). Modeling human multi-lineage heart field development with pluripotent stem cells. Cell Stem Cell *29*, 1382–1401.e8. https://doi.org/10.1016/j.stem.2022.08.007.
91. Horsthuis, T., Buermans, H.P.J., Brons, J.F., Verkerk, A.O., Bakker, M.L., Wakker, V., Clout, D.E.W., Moorman, A.F.M., 't Hoen, P.A.C., and Christoffels, V.M. (2009). Gene expression profiling of the forming atrioventricular node using a novel tbx3-based node-specific transgenic reporter. Circ. Res. *105*, 61–69. https://doi.org/10.1161/CIRCRESAHA.108.192443.
92. O'Rahilly, R. (1979). Early human development and the chief sources of information on staged human embryos. Eur. J. Obstet. Gynecol. Reprod. Biol. *9*, 273–280. https://doi.org/10.1016/0028-2243(79)90068-6.
93. Otis, E.M., and Brent, R. (1954). Equivalent ages in mouse and human embryos. Anat. Rec. *120*, 33–63. https://doi.org/10.1002/ar.1091200104.
94. Krishnan, A., Samtani, R., Dhanantwari, P., Lee, E., Yamada, S., Shiota, K., Donofrio, M.T., Leatherbury, L., and Lo, C.W. (2014). A detailed comparison of mouse and human cardiac development. Pediatr. Res. *76*, 500–507. https://doi.org/10.1038/pr.2014.128.
95. Anderson, K.P., Walker, R., Urie, P., Ershler, P.R., Lux, R.L., and Karwandee, S.V. (1993). Myocardial electrical propagation in patients with idiopathic dilated cardiomyopathy. J. Clin. Investig. *92*, 122–140. https://doi.org/10.1172/JCI116540.
96. Doshi, A.N., Walton, R.D., Krul, S.P., De Groot, J.R., Bernus, O., Efimov, I.R., Boukens, B.J., and Coronel, R. (2015). Feasibility of a semi-automated method for cardiac conduction velocity analysis of high-resolution activation maps. Comput. Biol. Med. *65*, 177–183. https://doi.org/10.1016/j.compbiomed.2015.05.008.
97. Lang, D., Holzem, K., Kang, C., Xiao, M., Hwang, H.J., Ewald, G.A., Yamada, K.A., and Efimov, I.R. (2015). Arrhythmogenic Remodeling of β_2 Versus β_1 Adrenergic Signaling in the Human Failing Heart. Circ. Arrhythm. Electrophysiol. *8*, 409–419. https://doi.org/10.1161/CIRCEP.114.002065.
98. Fu, Z., Dong, R., Zheng, H., Wang, Z., Cao, B., Bai, J., Ma, M., Song, Z., Pan, F., Xia, L., et al. (2024). Progress of Conductivity and Conduction Velocity Measured in Human and Animal Hearts. Rev. Cardiovasc. Med. *25*, 364. https://doi.org/10.31083/j.rcm2510364.
99. Tzatzalos, E., Abilez, O.J., Shukla, P., and Wu, J.C. (2016). Engineered heart tissues and induced pluripotent stem cells: Macro- and microstructures for disease modeling, drug screening, and translational studies. Adv. Drug Deliv. Rev. *96*, 234–244. https://doi.org/10.1016/j.addr.2015.09.010.
100. O'Shea, C., Holmes, A.P., Yu, T.Y., Winter, J., Wells, S.P., Correia, J., Boukens, B.J., De Groot, J.R., Chu, G.S., Li, X., et al. (2019). ElectroMap: High-throughput open-source software for analysis and mapping of cardiac electrophysiology. Sci. Rep. *9*, 1389. https://doi.org/10.1038/s41598-018-38263-2.
101. Kennedy, M., D'Souza, S.L., Lynch-Kattman, M., Schwantz, S., and Keller, G. (2007). Development of the hemangioblast defines the onset of hematopoiesis in human ES cell differentiation cultures. Blood *109*, 2679–2687. https://doi.org/10.1182/blood-2006-09-047704.
102. Kattman, S.J., Witty, A.D., Gagliardi, M., Dubois, N.C., Niapour, M., Hotta, A., Ellis, J., and Keller, G. (2011). Stage-Specific Optimization of Activin/Nodal and BMP Signaling Promotes Cardiac Differentiation of Mouse and Human Pluripotent Stem Cell Lines. Cell Stem Cell *8*, 228–240. https://doi.org/10.1016/j.stem.2010.12.008.
103. Laflamme, M.A., Chen, K.Y., Naumova, A.V., Muskheli, V., Fugate, J.A., Dupras, S.K., Reinecke, H., Xu, C., Hassanipour, M., Police, S., et al. (2007). Cardiomyocytes derived from human embryonic stem cells in pro-survival factors enhance function of infarcted rat hearts. Nat. Biotechnol. *25*, 1015–1024. https://doi.org/10.1038/nbt1327.
104. Wijsman, J.H., Jonker, R.R., Keijzer, R., Van De Velde, C.J., Cornelisse, C.J., and Van Dierendonck, J.H. (1993). A new method to detect apoptosis in paraffin sections: in situ end-labeling of fragmented DNA. J. Histochem. Cytochem. *41*, 7–12. https://doi.org/10.1177/41.1.7678025.
105. Andreatta, M., and Carmona, S.J. (2021). UCell: Robust and scalable single-cell gene signature scoring. Comput. Struct. Biotechnol. J. *19*, 3796–3798. https://doi.org/10.1016/j.csbj.2021.06.043.
106. Suo, S., Zhu, Q., Saadatpour, A., Fei, L., Guo, G., and Yuan, G.-C. (2018). Revealing the Critical Regulators of Cell Identity in the Mouse Cell Atlas. Cell Rep. *25*, 1436–1445.e3. https://doi.org/10.1016/j.celrep.2018.10.045.
107. Shannon, P., Markiel, A., Ozier, O., Baliga, N.S., Wang, J.T., Ramage, D., Amin, N., Schwikowski, B., and Ideker, T. (2003). Cytoscape: A Software Environment for Integrated Models of Biomolecular Interaction Networks. Genome Res. *13*, 2498–2504. https://doi.org/10.1101/gr.1239303.
108. Nunes, S.S., Miklas, J.W., Liu, J., Aschar-Sobbi, R., Xiao, Y., Zhang, B., Jiang, J., Massé, S., Gagliardi, M., Hsieh, A., et al. (2013). Biowire: a platform for maturation of human pluripotent stem cell–derived cardiomyocytes. Nat. Methods *10*, 781–787. https://doi.org/10.1038/nmeth.2524.
109. Sun, X., and Nunes, S.S. (2016). Biowire platform for maturation of human pluripotent stem cell-derived cardiomyocytes. Methods *101*, 21–26. https://doi.org/10.1016/j.ymeth.2015.11.005.
110. Williams, K., Liang, T., Massé, S., Khan, S., Hatkar, R., Keller, G., Nanthakumar, K., and Nunes, S.S. (2021). A 3-D human model of complex cardiac arrhythmias. Acta Biomater. *132*, 149–161. https://doi.org/10.1016/j.actbio.2021.03.004.

STAR★METHODS

KEY RESOURCES TABLE

REAGENT or RESOURCE	SOURCE	IDENTIFIER
Antibodies		
Mouse anti-CD140a – PE (PDGFRa)	BD Biosciences	Cat# 556002, RRID:AB_396286
Mouse anti-CD56-APC	BD Biosciences	Cat# 555518, RRID:AB_398601
Mouse anti-CD235ab-APC	BD Biosciences	Cat# 551336, RRID:AB_398499
Mouse anti-CD172a/b-PE-Cy7 (SIRPA)	BioLegend	Cat# 323808, RRID:AB_1236409
Mouse anti-CD90-APC	BD Biosciences	Cat# 559869, RRID:AB_398677
Mouse anti-Cardiac Troponin T (cTNT)	Thermo Fisher Scientific	Cat# MA5-12960, RRID:AB_11000742
Rabbit anti-Myosin Light Chain 2 (MLC2V)	Abcam	Cat# ab79935, RRID:AB_1952220
Mouse anti-Oct3/4A-PE	BD Biosciences	Cat# 561556, RRID:AB_10714783
Mouse anti-Sox2-PerCP-Cy5.5	BD Biosciences	Cat# 561506, RRID:AB_10646039
Goat anti-mouse IgG-APC	BD Biosciences	Cat# 550826, RRID:AB_398465
Donkey anti-rabbit IgG-PE	Jackson ImmunoResearch Labs	Cat# 711-116-152, RRID:AB_2340599
Donkey anti-rabbit IgG-A647	Thermo Fisher Scientific	Cat# A-31573, RRID:AB_2536183
Donkey anti-rabbit IgG-A555	Thermo Fisher Scientific	Cat# A-31572, RRID:AB_162543
Donkey anti-mouse IgG-A647	Thermo Fisher Scientific	Cat# A-31571, RRID:AB_162542
Donkey anti-mouse IgG-A555	Thermo Fisher Scientific	Cat# A-31570, RRID:AB_2536180
Rabbit anti-MSX2	Abcam	Cat# ab223692, RRID:AB_3083530
Rabbit anti-NKX2-5 (E1Y8H)	Cell Signaling Technology	Cat# 8792, RRID:AB_2797667
Mouse anti-Vimentin	Sigma-Aldrich	Cat# V6630, RRID:AB_477627
Rabbit anti-Ki67	Abcam	Cat# ab15580, RRID:AB_443209
Rabbit anti-Cleaved Caspase-3 (Asp175)	Cell Signaling Technology	Cat# 9661, RRID:AB_2341188
Biological samples		
Human fetal heart sample	Toronto Mount Sinai Hospital Research Centre for Women's and Infants' Health Biobank	N/A
Chemicals, peptides, and recombinant proteins		
G418	Thermo Fisher Scientific	Cat#10131035
FLP recombinase mRNA (mouse codon-optimized)	Miltenyi Biotec	Cat#130-106-769
DNA Polymerase 1 Large (Klenow) Fragment (TUNEL stain)	Promega	Cat# M2201
dATP, dCTP, dGTP (TUNEL stain)	Promega	Cat# U1201, U1211, U1221
Bio-11-dUTP (TUNEL stain)	Enzo	Cat# JBS-NU-803-BIOX-S
Gelatin	Sigma	Cat# G1890-100G
Matrigel	Thermo Fisher Scientific	Cat# CB40230
Matrigel without Phenol Red	Thermo Fisher Scientific	Cat# CB40230C
DMEMF/12	Thermo Fisher Scientific	Cat# MT-10-092-CV
StemPro-34	Thermo Fisher Scientific	Cat# 10639011
IMDM	Thermo Fisher Scientific	Cat# 12440061
IMDM without Phenol Red	Thermo Fisher Scientific	Cat# 21056023
Phosphate Buffered Saline (PBS)	Corning	Cat# MT21030CM
Fetal Bovine Serum (FBS)	FisherScientific	Cat# SH3039603
Bovine Serum Albumin (BSA)	Sigma	Cat# A1470
20% KnockOut Serum Replacement	Thermo Fisher Scientific	Cat# 10828028
L-glutamine	Thermo Fisher Scientific	Cat# 25030081
Non-Essential Amino Acids	Thermo Fisher Scientific	Cat# 11140050

(*Continued on next page*)

Continued

REAGENT or RESOURCE	SOURCE	IDENTIFIER
β-Mercaptoethanol	Thermo Fisher Scientific	Cat# 21985023
Penicillin/streptomycin	Thermo Fisher Scientific	Cat# 15070-063
Ascorbic Acid	Millipore Sigma	Cat# A4544
Transferrin	Millipore Sigma	Cat# 10652202001
Monothioglycerol	Millipore Sigma	Cat# M6145
Insulin-Transferrin-Selenium-Ethanolamine (ITS-X)	Thermo Fisher Scientific	Cat# 51500056
Recombinant human bFGF (FGF2)	Biotechne	Cat# 233-FB/CF
Recombinant human BMP4	Biotechne	Cat# 314-BP/CF
Recombinant human Activin A	Biotechne	Cat# 338-AC/CF
Recombinant human VEGF	Biotechne	Cat# 293-VE/CF
Recombinant human BMP2	Biotechne	Cat# 355-BM
SB-431542	Millipore Sigma	Cat# S4317
PD173074	Biotechne	Cat# 3044
CHIR99021	Biotechne	Cat# 4423
IWP2	Biotechne	Cat# 3533
Retinoic Acid	Millipore Sigma	Cat# R2625
ROCK inhibitor Y27632 (for all cell culture)	Selleckchem	Cat# S1049
ROCK inhibitor Y27632 (for eHTs only)	STEMCELL	Cat# 72304
LDN193189	Millipore Sigma	Cat# 260913
Insulin-like growth factor-1 (IGF-1)	BioTechne	Cat# 291-G1
DNase I	Millipore Sigma	Cat# 260913
poly-HEMA	Millipore Sigma	Cat# P3932
TrypLE	Thermo Fisher Scientific	Cat #12605010
Collagenase Type II	Worthington	Cat# 4176
CryoStor CS10 solution	StemCell Technologies	Cat# 100-1061
Triton X-100	Sigma	Cat# X100
Glycerin	Sigma	Cat# G2289
Normal donkey serum	Jackson (Cerdarlane)	Cat# 017-000-121
Hoescht	Thermo Fisher Scientific	Cat# H3570
DAPI	Thermo Fisher Scientific	Cat# D1306
ProLong Diamond Antifade Mounting Media	Thermo Fisher Scientific	Cat# P36965
Paraformaldehyde (PFA)	Cedarlane	Cat# 15710-S
Formalin	Sigma	Cat# F1635-1L
Agarose	Froggabio	Cat# A87-500G
Tris-HCl	Thermo Fisher Scientific	Cat# 15567-027
EDTA	Thermo Fisher Scientific	Cat# AM9260G
RNAseOUT	Thermo Fisher Scientific	Cat# 10777019
Fibrinogen	Sigma	Cat# F8630
Aprotnin	BioShop	Cat# APR600
RH237	Thermo Fisher Scientific	Cat# S1109
Methacholine	Sigma	Cat# A2251-25G
blebbistatin	Cayman Chemical	Cat# 13186-50
Cyclosporin A/Sandimmune IV	Novartis	Cat# 00593257
Pinacidil	Sigma	Cat# P154-100MG
Ketamine hydrochloride (Narketan)	Vetoquinol	Cat# DIN02374994
Xylazine (Rompun)	Elanco	Cat# DIN02169592
Meloxicam (Metcam)	Boehringer Ingelheim Animal Health	Cat# 02240463
Buprenophine-slow release (Vetergesic Mulidose)	CEVA Animal Health	Cat# DIN02342510

(*Continued on next page*)

Continued

REAGENT or RESOURCE	SOURCE	IDENTIFIER
Methylprednisolone (Solu-Medrol)	Pfizer	Cat# DIN02367971
Calcium chloride – $CaCl_2$	Fisher (Fluka)	Cat# 15641930
D-Glucose – dextrose anhydrous powder	Sigma	Cat# G8270
HEPES	Bioshop	Cat# 7365-45-9
Magnesium ATP – MgATP	Sigma	Cat# A9187
Magnesium chloride – $MgCl_2$	Fisher (Fluka)	Cat# 60047233
Magnesium sulfate – $MgSO_4$	Sigma	Cat# M1880
Potassium aspartate	Sigma	Cat# A6558
Potassium chloride – KCl	Sigma	Cat# P4504
Potassium phosphate monobasic – KH_2PO_4	Sigma	Cat P5655
Sodium Azide – NaN_3	Sigma	Cat# S2002
Sodium bicarbonate – $NaHCO_3$	Sigma	Cat# S5761
Sodium chloride – NaCl	Sigma	Cat# S0876
Sodium hydroxide – NaOH	Sigma	Cat# 221465
Sodium phosphate monobasic – NaH_2PO_4	Sigma	Cat# S0751
Sodium pyruvate – $C_3H_3NaO_3$	Sigma	Cat# P2256
Sucrose	Sigma	Cat# S0389
Critical commercial assays		
Amaxa 4D Nucleofector + P3 Primary Cell Solution	Lonza	Cat #V4XP-3034
ALDEFLUOR Kit	STEMCELL Technologies	Cat# 01700
RNAqueous-Micro Total RNA Isolation Kit	ThermoFisher	Cat# AM1931
Superscript III Reverse Transcriptase Kit	ThermoFisher	Cat# 18080044
QuantiNova SYBR Green PCR Kit	Qiagen	Cat# 208057
PSC-Derived Cardiomyocyte Isolation Kit	Miltenyi	Cat# 130-110-188
Fluo4 Membrane Potential Kit	ThermoFisher	Cat# F14201
Chromium Next GEM Single Cell 3′ Kit v3.1	10x Genomics	Cat# PN-1000268
Deposited data		
hPSC-derived AVNLPC scRNA-seq	This Manuscript	NCBI GEO: GSE297072
Fetal AVN snRNA-seq	This Manuscript	NCBI GEO: GSE297073
Adult snRNA-seq[55]	Kanemaru et al.	ArrayExpress: E-MTAB-12916
scRNA-seq MERFISH dataset[54]	Farah et al.	CIRM CESCG: chiCardiomyocyte1
Experimental models: Cell lines		
Human ESC: HES3-Nkx2-5$^{egfp/w}$ line[43]	Gift from Dr. E Stanley, Monash University, AU	N/A
Human ECS: HES3-Nkx2-5$^{egfp/w}$ TBX3$^{tdtom/w}$ reporter cell line	This Manuscript	N/A
Human ESC: HES2 line[52]	WiCell	Cat# ES02, RRID:CVCL_D093
Human ESC: ESI-017 ASAP1 cell line[51]	Gift from Dr. M. Laflamme, University Health Network, CA; Dhahri et al.	N/A
DR4 Mouse Embryonic Fibroblasts (irradiated)	ThermoFisher	Cat# A34966
NHCF-V – Human Ventricular Cardiac Fibroblasts	Lonza	Cat# CC-2904
Experimental models: Organisms/strains		
Male Hartley Guinea Pigs (650-700g)	Charles River Laboratories	N/A
Oligonucleotides		
Primers for genotyping, see Table S5	This Manuscript	N/A
Primers for qRT-PCR, see Table S5	This Manuscript	N/A

(*Continued on next page*)

Continued

REAGENT or RESOURCE	SOURCE	IDENTIFIER
Recombinant DNA		
TALEN plasmids targeting TBX3 locus	Cellectis Bioresearch	Custom plasmid; sequence available upon request
Targeting vector (TBX3-tdTomato)	GENEArt, Thermo Fisher Scientific	Custom plasmid; sequence available upon request
Software and algorithms		
ImageJ (FIJI)	https://imagej.net/software/fiji/	RRID: SCR_002285
HALO HighPlex FL v4.1.5944.283 image analysis platform	Indica Labs; https://indicalab.com/halo/halo-modules/highplex-fl/	RRID: SCR_018350
pCLAMP	Molecular Devices; https://www.moleculardevices.com/products/axon-patch-clamp-system/acquisition-and-analysis-software/pclamp-software-suite	RRID: SCR_011323
FlowJo v10.10	BD Biosciences; https://www.flowjo.com/flowjo/overview	RRID: SCR_008520
GraphPad Prism 10.4.1	GraphPad; https://www.graphpad.com/	RRID: SCR_002798
CellRanger	10x Genomics; https://www.10xgenomics.com/	RRID: SCR_017344
RStudio	https://posit.co/download/rstudio-desktop/	RRID:SCR_000432
Seruat version 5.0.1	https://satijalab.org/seurat/	RRID:SCR_016341
UCell	https://github.com/MarcAndreatta/UCell	RRID: SCR_027109
Python Programming Language	https://www.python.org/	RRID:SCR_008394
Leica Application Suite X	https://www.leica-microsystems.com/products/microscope-software/p/leica-las-x-ls/	RRID:SCR_013673
NIS-Elements Software	Nikon; https://www.microscope.healthcare.nikon.com/products/software/nis-elements	RRID:SCR_014329
Zeiss Zen Microscopy Software	Carl Zeiss Microscopy; https://www.zeiss.com/microscopy/en/products/software/zeiss-zen.html	RRID:SCR_013672
Database for Annotation, Visualization, and Integrated Discovery (DAVID) Bioinformatics Resources version Dec. 2021	https://david.ncifcrf.gov/	RRID:SCR_001881
BrainVision Analyzer	https://www.brainproducts.com/solutions/analyzer/	RRID:SCR_002356
Electromap (MATLAB)	https://github.com/CXO531/ElectroMap; From O'Shea Lab[100]	N/A
Labchart	ADInstruments; https://www.adinstruments.com/products/labchart/versions-and-licenses	RRID:SCR_023643
Metamorph	Molecular Devices; https://www.moleculardevices.com/products/cellular-imaging-systems/high-content-analysis/metamorph-microscopy	RRID:SCR_002368
Custom MATLAB scripts	From Laflamme Lab; Dhahri et al.[51]	N/A
PowerLab 8/35 Data Acquisition System	AD Instruments; https://m-cdn.adinstruments.com/owners-guides/PowerLab%20SP%20Series%20OG.pdf	RRID:SCR_018833
Adobe Illustrator	http://www.adobe.com/products/illustrator.html	RRID:SCR_010279
Biorender	http://biorender.com	RRID:SCR_018361

(*Continued on next page*)

Continued

REAGENT or RESOURCE	SOURCE	IDENTIFIER
Other		
12mm coverslips	FisherScientific	Cat# 22293232P
Douncer	Sigma	Cat# D9063
FTS BioCool Controlled Rate Freezer	Scientific Products	N/A
BD LSRFortessa Cell Analyzer	BD Biosciences	RRID:SCR_018655
Beckman Coulter CytoFLEX Flow Cytometer	Beckman Coulter	RRID:SCR_019627
BD FACSAria II Cell Sorter	BD Biosciences	RRID:SCR_018934
Nikon A1R confocal microscope	Nikon Instruments	N/A
Leica SP8 confocal microscope	Leica Microsystems	N/A
AXIO microscope	ZEISS	N/A
EVOS microscope	ThermoFisher	N/A
Zeiss Axio Observer Z1 microscope with PECON incubation chamber and O_2 control module	ZEISS / PeCon	N/A
NovaSeq 6000 Sequencing System	Illumina	N/A
Axopatch 200B	Molecular Devices	N/A
DigiData	Molecular Devices	N/A
Complementary metal-oxide semiconductor (CMOS) camera Ultima-L	Ultima-L, Scimedia	N/A
MVX-10 Olympus fluorescence microscope	Olympus	N/A
Mercury arc source	X-Cite Exacte	N/A
480nm filter cube	Olympus	U-MWIG2
Heated plate	Olympus	MATS-U55S
Micromanipulator	World Precision Instruments	N/A
Stimulator	Grass S88X	N/A
Bioamplifier	AD Instruments	Model ML136
Collimating lens	Navitar	25 mm, N.A. 0.05, W.D. 10mm
Dichroic system	Photometrics	DC2 dual-channel splitter
EMCCD cameras	Photometrics	Evolve128
LED spotlights with Chroma ET470/40x filters	Mightex	PLS-0470-030-15-S
Bipolar electrode made of two fine silver wires	Hardware store	AWG#32
Magnetic stand with a ball joint	World Precision Instruments	N/A

EXPERIMENTAL MODEL AND STUDY PARTICIPANT DETAILS

Human ESC lines

All human pluripotent stem cell (hPSC) research conducted in this study was approved by the Stem Cell Oversight Committee of the Canadian Institutes of Health Research and by UHN's Research Ethics Board. The HES3-Nkx2-5$^{egfp/w}$ TBX3$^{tdtom/w}$ reporter cell line (karyotype: 46, XX)[43] was generated as detailed in the methods section below. The HES2 cell line (karyotype: 46, XX)[52] was purchased from WiCell. The ESI-017-ASAP1 cell line (karyotype: 46, XX)[51] was generously provided by Dr. Michael Laflamme.

Generation of the HES3-Nkx2-5$^{egfp/w}$ TBX3$^{tdtomato/w}$ hPSC line

The HES3 NKX2-5$^{eGFP/wt}$ human embryonic stem cell (hESC) line was a kind gift from Prof. E. Stanley (Monash University, Victoria, AU).[43] The introduction of the tandem dimer tomato (tdTomato) fluorescence reporter gene into the TBX3 locus of this cell line was performed by the Centre for Commercialization of Regenerative Medicine, Toronto. TALEN pairs were designed and tested for cutting efficiency in collaboration with Cellectis bioresearch, France. The left and right DNA binding TALEN sequences were cloned in two separate backbones by Cellectis bioresearch and sequence verified. TALENS were selected based on cutting efficiency and to target the endogenous start codon (ATG) of TBX3 to incorporate the tdTomato fluorescence gene (Figure S1A). The targeting vector comprised of: 1kb homology arms on each side of the endogenous start codon of TBX3, coding sequence of tdTomato, a polyadenylation signal followed by a FRT flanked Neomycin selection cassette under a ubiquitous human phosphoglycerate kinase promoter (hPGK). The sequence "AGCCTCTCCATGAGAGATCCG" was removed from targeting vector to prevent TALEN binding and cutting

of the targeting vector. The targeting vector was gene synthesized by GENEART (ThermoFisher Scientific), endotoxin free maxi prepped and sequence verified.

For transgene delivery, HES3 NKX2-5$^{eGFP/wt}$ cells were trypsinized with TrypL (ThermoFisher, 12605010) into a single cell suspension and 800,000 cells were electroporated with 2.5 μg each of the two TALEN plasmids along with 2 μg of targeting vector using the DN100 program of an Amaxa 4D Nucleofector and P3 primary cell solution (Lonza, V4XP-3034). The electroporated cells were plated onto drug resistant Irradiated DR4 Mouse embryonic fibroblasts (ThermoFisher, A34966) in three 10-cm cell culture dishes and successfully targeted hESCs were selected using G418 treatment (ThermoFisher, 10131035).

Clones with heterozygous edited TBX3 gene locus were identified by PCR screening and confirmed using Sanger sequencing (1st targeting primers, Table S5). To remove the neomycin selection cassette, a successfully edited HES3 NKX2-5$^{eGFP/wt}$ clone was transfected with an *in vitro* transcribed mouse codon optimized FLP recombinase mRNA (Miltenyi Biotec, 130-106-769). Excision of the neomycin selection cassette was confirmed via PCR and sanger sequencing (Selection cassette removal primers, Table S5).

The final NKX2-5$^{eGFP/wt}$ TBX3$^{tdTomato/wt}$ hESC clones (#5 and #7) were subjected to Mycoplasma testing (negative). Normal karyotype (46, XX) was confirmed by Standard G banding karyotyping by the Institute of Human Genetics, University Clinic Jena, Germany (Figure S1C). Pluripotency was confirmed via flow cytometry using anti-Oct3/4-PE (BD, 561556), anti-Sox2-PerCP-Cy5.5 (BD, 561506) (Figure S1D). Brightfield and fluorescence imaging was used to confirm GFP and tdTomato reporter expression in NKX2-5$^{eGFP/wt}$ TBX3$^{tdTomato/wt}$ hESCs differentiated into cardiomyocyte subtypes using an EVOS Microscope (ThermoFisher) (Figures S1F and S3B).

Human pluripotent stem cell maintenance

Human pluripotent stem cell lines were cultured as described previously.[101] Briefly, cells were maintained as monolayers on a 0.1% gelatin (Sigma, G1890) and 0.1% Matrigel (FisherScientific, CB40230) matrix with irradiated mouse embryonic fibroblasts (ThermoFisher, A34966) in DMEMF/12 (ThermoFisher, MT-10-092-CV) supplemented with 20% KnockOut serum replacement (ThermoFisher, 10828028), 2 mM L-glutamine (ThermoFisher, 25030081), 1x non-essential amino acids (ThermoFisher, 11140050), 55 mM β-mercaptoethanol (ThermoFisher, 21985023) and 1% penicillin/streptomycin (ThermoFisher, 15070-063), and 20 ng/mL recombinant human (rh)-bFGF (Biotechne, 233-FB/CF). All hPSC lines had normal karyotypes and tested negative for mycoplasma.

Use of human fetal tissue

Human fetal heart sample from gestation weeks 19 was provided by the Toronto Mount Sinai Hospital Research Centre for Women's and Infants' Health Biobank. The use of human fetal tissue in this study was approved by the Research Ethics Boards of both Mount Sinai Hospital, Toronto, and the UHN, Toronto. Samples were obtained from voluntary pregnancy terminations. After patients signed the standard consent form for the procedure, they were approached by the Mount Sinai Hospital Research Centre for Women's and Infants' Health BioBank to request consent for the donation of fetal tissue. Donors were fully informed about the intended research use of the samples and did not receive compensation for their donation. Fetuses with chromosomal abnormalities, cardiovascular defects, or from mothers with congenital heart defects, arrhythmias, diabetes (type 1, type 2, or gestational), or Systemic Lupus Erythematosus were excluded from the study to ensure the inclusion of healthy heart samples. The fetal sex was not specified for this study and not included in the health information shared with the study team.

Use of Animals

Guinea Pig use in experimental studies

Male Hartley guinea pigs (650–700 g, Charles River) were used, with all procedures performed in accordance with and approved by the Animal Use and Care Committee at UHN. Surgeries were performed under ketamine (35 mg/kg, Vetoquinol, DIN02374994) and xylazine (2 mg/kg, Elanco, DIN02169592) induction and isoflurane maintenance, with orotracheal intubation and mechanical ventilation. Meloxicam (0.2 mg/kg, Boehringer Ingelheim Animal Health, 02240463) and Buprenorphine-slow release (0.7–1.2 mg/kg, CEVA Animal Health, DIN02342510) were administered for pain management. Animals were placed on a 38°C water blanket to maintain body temperature, O2 saturation and heart rate were monitored using a toe probe. The surgical site was prepared with betadine, and ophthalmic ointment was applied to prevent corneal drying. Postoperatively, animals received subcutaneous saline (5 mL) and were monitored in a warm environment until full recovery. They were assessed daily for the first week, then biweekly, with immunosuppressed animals weighed and examined daily. Veterinary services were consulted if signs of severe distress, infection, or >20% weight loss were observed.

METHOD DETAILS

Directed Differentiation of Human ESC Lines

To differentiate hPSCs into cardiomyocytes, we employed our previously reported embryoid body (EB)-based protocol.[26,29,102] For all differentiation steps, the base media consisted of either 100% StemPro-34 media (ThermoFisher, 10639011) or 20% StemPro-34 media diluted with IMDM (ThermoFisher, 12440061). Base media was supplemented with 1% penicillin/streptomycin, 2 mM L-glutamine, 50 μg/mL ascorbic acid (MilliporeSigma, A4544), 75 μg/mL transferrin (MilliporeSigma, 10652202001), and 50 μg/mL monothioglycerol (MilliporeSigma, M6145). hPSC colonies were grown to ~80% confluence and dissociated into single cells using TrypLE (ThermoFisher, 12605010). Cells were aggregated for 18 hours on an orbital shaker at 70 rpm (ESI-017-ASAP1) or 80 rpm (HES3,

HES2) in 6-cm low-attachment dishes at a concentration of $0.5x10^6$ cells/mL. Cells were suspended in 20% StemPro-34 base media supplemented with 0.01x ITS-X (ThermoFisher, 51500056), 1 ng/mL rhBMP4 (Biotechne, 314-BP/CF), 10μM ROCK inhibitor Y27632 (Selleckchem, S1049), and 250 U/mL DNase I (MilliporeSigma, 260913). EBs were incubated in a low oxygen environment (5% CO_2, 5% O_2, 90% N_2) until day 11 and then in a 5% CO_2 ambient air environment thereafter. The EBs were kept in tissue culture plastic pre-coated with 5% (w/v) poly-HEMA (MilliporeSigma, P3932) throughout the differentiation to maintain suspension cultures.

Generation of VLCMs

On day 1 of differentiation, EBs were transferred to ventricular mesoderm induction media consisting of cardiac base media: 100% StemPro-34 supplemented with 1 μM CHIR99021 (Biotechne, 4423), 2.5 ng/mL rhbFGF, 10 ng/mL rhBMP4, and 8 ng/mL rhActivin A (Biotechne, 338-AC/CF). On day 3, EBs were washed with IMDM and suspended in cardiac induction media containing 100% StemPro-34 with 1 μM IWP2 (Biotechne, 3533) and 10 ng/mL rhVEGF (Biotechne, 293-VE/CF). On day 5, the media was replaced with cardiac maintenance media: 20% StemPro-34 and 5 ng/mL rhVEGF. Starting from day 11, EBs were cultured in maintenance media without rhVEGF. Media changes were performed every 3–4 days.

Generation of ALCMs

At day 1 of differentiation the EBs were transferred to atrial mesoderm induction media consisting of: cardiac base media of 100% StemPro-34 with 1 μM CHIR99021, 2.5 ng/mL rhbFGF, 3 ng/mL rhBMP4, and 2 ng/mL rhActivin A. At day 3 the EBs were washed with IMDM and suspended in cardiac induction media (as described for VLCMs) with the addition of 0.5 μM retinoic acid (MilliporeSigma, R2625). From day 5 onward, media changes were performed as described for VLCMs.

Generation of SANLPCs

On day 1 of differentiation, embryoid bodies (EBs) were transferred to SAN pacemaker mesoderm induction media composed of cardiac base media (100% StemPro-34) supplemented with 1 μM CHIR99021, 2.5 ng/mL rhbFGF, 3 ng/mL rhBMP4, and 2 ng/mL rhActivin A. On day 3, EBs were washed with IMDM and transitioned to SAN pacemaker induction media containing 0.5 μM IWP2, 10 ng/mL rhVEGF, 2.5 ng/mL rhBMP4, 1.5 μM SB-431542 (MilliporeSigma, S4317), and 0.125 μM retinoic acid. On day 4, 1000 nM PD173074 (Biotechne, 3044) was added to the media. Starting on day 6, cells were cultured in base media consisting of 100% StemPro-34 supplemented with 5 ng/mL rhVEGF. From day 8 onward cells were cultured in cardiac maintenance media and media changes were performed as described for VLCMs.

Generation of AVNLPCs

At day 1 of differentiation the EBs were transferred to AVN pacemaker mesoderm induction media consisting of: cardiac base media of 100% StemPro-34 with 1 μM CHIR99021, 2.5 ng/mL rhbFGF, and 5 ng/mL rhBMP4 + 4 ng/mL rhActivin A (HES3) or 5 ng/mL rhBMP4 + 2 ng/mL rhActivin A (HES2, ESI-017-ASAP1). Please note, mesoderm induction conditions, especially BMP4 and activin A concentrations, have to be optimized for every cell line due to varying endogenous signaling between cell lines. At day 3 the EBs were washed with IMDM and suspended in cardiac induction media (as described for VLCMs). For BMP2-induced AVNLPCs: 200 ng/mL rhBMP2 (Biotechne, 355-BM) was added to the cardiac maintenance media at either day 5 (HES3) or day 8 (HES2, ESI-017-ASAP1) of differentiation. At day 8 (HES3) or 11 (HES2, ESI-017-ASAP1) of differentiation and thereafter, media was changed as described for VLCMs. For CHIR-induced AVNLPCs: 12 μM CHIR99021 was added to the cardiac maintenance media at either day 8 (HES3) or day 11 (HES2 and ESI-017-ASAP1) of differentiation in cardiac maintenance media. At day 11 (HES3) or 15 (HES2, ESI-017-ASAP1) of differentiation and thereafter, media was changed as described for VLCMs.

Aggregation experiments: To examine the effects of BMP and Wnt signaling on AVNLPC development, embryoid bodies (EBs) were dissociated into single cells on either day 5 or day 8. Day 5 EBs were dissociated using TrypLE, while day 8 EBs were treated with Collagenase Type II (1 mg/mL, Worthington, 4176) in Hank's buffer (NaCl, 136 mM; $NaHCO_3$, 4.16 mM; Na_3PO_4, 0.34 mM; KCl, 5.36 mM; KH_2PO_4, 0.44 mM; dextrose, 5.55 mM; HEPES, 5 mM). To promote aggregate formation, cells were cultured at high density (75,000 cells/well) in 96-well ultra-low attachment plates. Cells were cultured in cardiac induction media supplemented with 10 μM ROCK inhibitor and the indicated concentrations and combinations of rhBMP2, CHIR99021, and LDN193189 (Biotechne, 6053). After 4 days the aggregates were transferred to 24-well plates pre-coated with 5% (w/v) poly-HEMA and cultured in cardiac maintenance media as described above.

Cardiomyocyte cryopreservation

To enhance engraftment and cell survival of transplanted cardiomyocytes *in vivo*, EBs were subjected to heat shock and a pro-survival cocktail before cryopreservation as previously described.[103] The heat shock process involved a 1-hour incubation at 42°C, followed by a 3- to 5-hour incubation at 37°C in cardiac maintenance media supplemented with 100 nM insulin-like growth factor-1 (IGF-1) (Biotechne, 291-G1). and 200 nM cyclosporine A/Sandimmune IV (Novartis, 00593257). EBs were dissociated overnight a RT with Collagenase Type II in Hank's buffer as described above and then resuspended in CryoStor CS10 solution (StemCell Technologies, 100-1061) for preservation using a Controlled-Rate Freezer (Bio-Cool), as detailed in previous reports.[81]

RNA Isolation and Quantitative Real-Time PCR

Total RNA was extracted from hPSC-derived cardiomyocytes using the RNAqueous-Micro Total RNA Isolation Kit (ThermoFisher, AM1931), including RNase-free DNase treatment. Complementary DNA (cDNA) synthesis was performed using Superscript III Reverse Transcriptase (ThermoFisher, 18080044) with oligo(dT) primers and random hexamers. Quantitative reverse transcription PCR (RT-qPCR) was conducted using the QuantiNova SYBR Green PCR Kit (Qiagen, 208057) on a QuantStudio5 RT-qPCR machine (ThermoFisher), following the manufacturer's instructions. All reactions were prepared in duplicate. As previously described, a tenfold

serial dilution of human genomic DNA standards (30 ng/mL to 3.0 pg/mL) was included in each experiment to verify PCR efficiency and calculate the relative copy number of each target gene normalized to the housekeeping gene TBP.[44] Primer sequences are detailed in Table S5. To facilitate visualization and comparison of expression patterns, the data were log2-transformed and displayed as a heatmap.

Flow Cytometry and Cell Sorting

EBs at day 1–8 of differentiation were dissociated using TrypLE for 3–6 minutes at 37°C. Day 10–50 EBs were dissociated using Collagenase type II in Hank's buffer as detailed above for 16 hours at room temperature. If necessary, this was followed by further dissociation with TrypLE.

For surface marker staining, cells were incubated with antibodies for 30 minutes at 4°C in PBS (Corning, MT21030CM) containing 5% Fetal Bovine Serum (FBS) (FisherScientific, SH3039603) and 0.02% sodium azide (Sigma, S2002).The following conjugated antibodies were used for staining: anti-PDGFRα-PE (BD Biosciences, 556002, 6:100), anti-CD56-APC (BD Biosciences, 555518, 1:100), anti-CD235ab-APC (BD Biosciences, 551336, 1:100), anti-CD172a/b-PE-Cy7 (SIRPA; BioLegend, 323808, 1:1000), anti-CD90-APC (BD Biosciences, 559869, 1:300). Detailed antibody information is provided in the key resources table. Prior to acquisition, cells were suspended in FACS buffer containing DAPI (Thermo Fisher Scientific, D1306; 1:10,000) for live/dead discrimination.

For intracellular staining, cells were fixed with 4% paraformaldehyde (PFA) (Cedarlane, 15710-S) for 10 minutes at 4°C. Staining was performed in PBS containing 0.3% bovine serum albumin (BSA, Sigma, A1470) and 0.3% Triton X-100 (Sigma, X100). Cells were incubated with primary antibodies overnight at 4°C, followed by a 30-minute incubation with secondary antibodies at 4°C. The following primary antibodies were used for staining: anti-OCT3/4-PE (BD Biosciences, 561556, 1:300), anti-SOX2-PerCP-Cy5.5 (BD Biosciences, 561506, 1:100), mouse anti-cardiac troponin T (cTNT; Thermo Fisher Scientific, MA5-12960, 1:2000), and rabbit anti-myosin light chain 2 ventricular isoform (MLC2v; Abcam, ab79935, 1:1000). The following secondary antibodies were used for detection of cTNT and MLC2v: goat anti-mouse IgG-Alexa Fluor 647 (BD Biosciences, 550826, 1:500) and donkey anti-rabbit IgG-PE (Jackson ImmunoResearch, 711-116-152, 1:500). Detailed antibody information is provided in the key resources table.

After staining, cells were analyzed using either a LSRFortessa (BD) or a Cytoflex (Beckman Coulter) flow cytometer. Flow cytometric analysis was conducted using FlowJo software (BD).

The proportion of NKX2-5$^+$TBX3$^+$ cardiomyocytes (AVNLPCs) out of total cells was calculated by multiplying the proportion of SIRPA$^+$CD90$^-$ cardiomyocytes with the proportion of NKX2-5$^+$TBX3$^+$ cells gated out of the SIRPA$^+$CD90$^-$ gate.

For fluorescence-activated cell sorting, cells were suspended in IMDM with 0.5% fetal calf serum (FCS) and sorted at a concentration of 10 million cells/mL using a FACS Aria sorter (BD) at the SickKids-UHN Flow Cytometry Facility. Magnetic-activated cell sorting (MACS) to isolated cardiomyocytes was performed using the PSC-Derived Cardiomyocyte Isolation Kit (Miltenyi, 130-110-188) according to the manufacturer's protocol.

Immunohistochemistry

Monolayer staining

Day 25 EBs were dissociated as described above and then cardiomyocytes were plated onto Matrigel (25% v/v, FisherScientific, CB40230) coated 12 mm coverslips (FisherScientific, 22293232P) and cultured in cardiac maintenance media supplemented with 10 μM ROCK inhibitor Y27632 (Selleckchem, S1049). After 48 hours, cells were transferred to cardiac maintenance media without ROCK inhibitor and then cultured for another 2–4 days until confluent. Monolayers were fixed with 4% PFA for 10 minutes at 4°C and then permeabilized in PBS containing 0.3% Triton X-100 and 200 mM glycerin (Sigma, G2289) for 20 minutes at room temperature (RT). Following permeabilization, samples were blocked using blocking buffer (PBS containing 10% donkey serum, 2% BSA, and 0.3% Triton X-100) for 30 minutes at RT. The following primary antibodies were used for staining: mouse anti-cardiac troponin T (cTNT; Thermo Fisher Scientific, MA5-12960, 1:200), rabbit anti-myosin light chain 2 ventricular isoform (MLC2V; Abcam, ab79935, 1:100), rabbit anti-MSX2 (Abcam, ab223692, 1:300), rabbit anti-NKX2-5 (Cell Signaling Technology, 8792S, 1:800), mouse anti-Vimentin (Sigma-Aldrich, V6630, 1:100), rabbit anti-Ki67 (Abcam, ab15580, 1:300), and rabbit anti-Cleaved Caspase-3 (Asp175; Cell Signaling Technology, 9661, 1:400). Detailed antibody information is provided in the key resources table. Primary antibodies were diluted in staining buffer (PBS containing 1% normal donkey serum (Jackson Cerdarlane, 017-000-121) and 0.3% Triton X-100), applied to the samples and incubated overnight at 4°C. The samples were then washed three times with wash buffer (PBS containing 0.1% BSA and 0.1% Triton X-100). For detection of unconjugated primary antibodies, the following secondary antibodies were used: donkey anti-rabbit IgG-Alexa Fluor 647 (Thermo Fisher Scientific, A31573, 1:500), donkey anti-rabbit IgG-Alexa Fluor 555 (Thermo Fisher Scientific, A31572, 1:500), donkey anti-mouse IgG-Alexa Fluor 647 (Thermo Fisher Scientific, A31571, 1:500), or donkey anti-mouse IgG-Alexa Fluor 555 (Thermo Fisher Scientific, A31570, 1:500). Detailed antibody information is provided in the key resources table. Secondary antibodies were applied in staining buffer along with 10 μg/mL Hoechst (FisherScientific, H3570) for 1 hour at RT. Afterwards, the samples were washed three times with wash buffer, and once with distilled water before mounting with ProLong Diamond Antifade Mounting Media (FisherScientific, P36965).

Tissue section staining

Engineered heart tissues were fixed in 4% formalin (Sigma, F1635-1L) for 30 minutes at room temperature and embedded in 1% agarose (Froggabio, A87-500G). Guinea pig hearts were fixed overnight at 4°C in 4% formalin. Following fixation, all tissue samples were transferred to 70% ethanol and sent to the UHN Pathology Research Program for paraffin embedding and sectioning into 5-μm thick slices. For immunofluorescence staining, tissue sections were rehydrated using xylene and a graded ethanol series, followed by

heat-induced antigen retrieval in citrate buffer (pH 6). Blocking was performed in PBS containing 10% donkey serum and 0.1% Triton X-100. The sections were then incubated with primary antibodies overnight at 4°C. Detailed antibody information is described above and in the key resources table. After three PBS washes, secondary antibodies and 10 μg/mL Hoechst were applied in PBS with 0.1% Tween for 1 hour at room temperature. Finally, the samples were washed three times with PBS, and once with distilled water, and mounted using ProLong Diamond Antifade Mounting Media. TUNEL staining was performed by the UHN Pathology Research Program according to a previously described protocol.[104] Briefly, sections were processed using DNA Polymerase I Large (Klenow) Fragment (Promega, M2201), deoxynucleotide triphosphates (dATP, dCTP, dGTP; Promega, U1201, U1211, U1221), and Bio-11-dUTP (Enzo, JBS-NU-803-BIOX-S) to label fragmented DNA ends.

Imaging

All samples were imaged at the Advanced Optical Microscopy Facility at UHN. Monolayers were imaged using the Nikon A1R confocal microscope with 20x/0.75 NA and 40x/0.85 NA objectives, along with the NIS-Elements software. Section stains were imaged using the Leica SP8 with a 20x/0.75 NA objective and controlled via the LAS X software. Image processing and preparation were carried out using ImageJ (FIJI). Fluorescent images were quantified using HALO HighPlex FL v4.1.5944.283 image analysis platform (Indica Labs) for automated cell segmentation and marker detection (cTNT, NKX2-5, Vimentin, Ki67, Cleaved Caspase-3), or ImageJ for thresholding and intensity analysis (MSX2 and TUNEL). Regions of interest were defined based on Hoechst-stained nuclei.

Single Cell Patch Clamp

To perform electrophysiological characterization using patch clamp recordings specific cell populations were isolated via FACS as described. Cells were resuspended at a concentration 1.25–5 $\times$ 10^6 cells/mL in cardiac maintenance media (without VEGF) containing 10 μM ROCK inhibitor Y27632 (Selleckchem, S1049) and filtered through a 70 μm filter. 40 μL drops of this suspension were plated onto 3 $\times$ 5 mm Matrigel-coated (10% v/v) glass coverslips in 30 mm dishes and incubated for 16-18 hours to facilitate cell attachment. Then, dishes were flooded with 2 mL of fresh media. Media was changed every four days, and recordings were performed 5–14 days post-plating.

Action potentials and membrane currents were recorded using standard patch clamp techniques in current- and voltage-clamp modes (Axopatch 200B, Molecular Devices). Signals were acquired at 5 kHz (DigiData, Molecular Devices) and analyzed with pCLAMP software (Molecular Devices). Borosilicate glass microelectrodes with tip resistances of 2-5 MΩ were used, with series resistance compensated by ~70%.

Spontaneous action potentials and funny current (I_f) were recorded at 37°C using the perforated patch method (nystatin). The bath solution contained (mM): 124 NaCl, 5.4 KCl, 1.2 $CaCl_2$, 1 $MgCl_2$, 5 glucose, and 10 HEPES (pH 7.4, NaOH). The pipette solution contained (mM): 120 potassium aspertate, 20 KCl, 5 NaCl, 1 $MgCl_2$, 5mM MgATP, and 10 HEPES (pH 7.2, KOH). I_f was elicited by 3-second voltage steps from −40 mV to −120 mV (10 mV increments) from a -40 mV holding potential. Current density was calculated by subtracting the instantaneous current (t = 0) from the steady-state current at the end of each voltage step.

Beat rate analysis

Beat rates were quantified from FACs-sorted single cardiomyocytes and embryoid bodies (EBs) in cardiac maintenance media. FACs-isolated single cells were plated as described for single-cell patch-clamp experiments, except that cells were seeded onto Matrigel-coated tissue culture plastic rather than glass coverslips. EBs were maintained in suspension and analyzed directly in culture medium. Spontaneous beating was recorded using a Zeiss Axio Observer Z1 inverted microscope equipped with a PECON incubation chamber (37°C, 5% CO_2), operated using Zeiss Zen software. Videos were acquired for approximately 30 seconds, beat rates were calculated manually from recorded videos and presented as beats per minute.

Single-Cell/Nucleus RNA Sequencing

Isolation and processing of fetal tissue for snRNA-seq

To obtain AVN fetal tissue for single-nucleus RNA sequencing (snRNA-seq), we dissected the lower right atrium near the atrial-ventricular boundary from a fetal heart at 19 weeks of gestation. The tissue was immediately submerged in liquid nitrogen for rapid freezing and subsequently stored at −80°C. For processing, the tissue was dissociated in a lysis buffer composed of 0.32 M sucrose (Sigma, S0389), 5 mM $CaCl_2$ (Fluka, 21114), 3 mM $Mg(AC)_2$ (Sigma, 228648), 20 mM Tris-HCl (ThermoFisher, 15567-027), 0.1% Triton X-100 (MilliporeSigma, X100), and 0.1 mM EDTA (ThermoFisher, AM9260G) prepared in DNase/RNase-free water (Qiagen, 129115). The tissue was mechanically homogenized with a douncer (Sigma, D9063) to yield single nuclei, which were then washed twice with PBS containing 1% BSA and 0.2 U/μl RNAseOUT (ThermoFisher, 10777019) and filtered through a 40 μm cell strainer. Finally, the nuclei were stained with DAPI (10 μg/mL) and sorted for $DAPI^+$ single nuclei using a FACSAria (BD) at the SickKids-UHN Flow Cytometer Facility.

Isolation and Processing of AVNLPCs for scRNA-seq

To perform single-cell RNA sequencing (scRNA-seq) on BMP2 AVNLPCs derived from the HES2 cell line, embryoid bodies (EBs) were dissociated into a single-cell suspension on day 25 of differentiation using the methods described above. The cells were then resuspended in 1X PBS containing 0.04% BSA and filtered through a 40-μm cell strainer.

Raw data processing, quality control and clustering

Both single-cell and single-nucleus suspensions were prepared for sequencing using the 10x Genomics Chromium platform with the Single Cell 3' v3 reagent kit. The resulting libraries were sequenced on an Illumina NovaSeq 6000, collecting over 45,000 reads per cell. Raw data were processed with the 10x Genomics CellRanger pipeline at UHN's Princess Margaret Genomics Centre. For mapping, single-cell RNA-seq data were aligned to the human reference genome GRCh38, while single-nucleus RNA-seq data were aligned to GRCh38-premrna. All downstream analyses were performed in R using the Seurat toolkit. (version 5.0.1, https://satijalab.org/seurat/.) First, low-quality cells and potential doublets were filtered out. Specifically, cells with a library size below (10000 for hPSC and 3000 for fetal) or above 50,000 were excluded. Additionally, we removed damaged cells by applying mitochondrial gene expression thresholds (fetal snRNA-seq: 0.75% and hPSC scRNA-seq: 13.093%). The remaining data was then normalized using SCTransform. Next, we performed principal component analysis with RunPCA and selected the top 25 principal components for further clustering via the FindClusters function. The final cluster resolutions were set at 0.2 (full dataset) and 1.4 (cardiomyocyte subcluster) for the fetal snRNA-seq dataset and 0.1 (full dataset) and 0.5 (cardiomyocyte subcluster) for the hPSC scRNA-seq dataset.

Differential gene expression analysis

To identify differentially expressed genes (DEGs) within each cluster we employed the FindAllMarkers function with the following parameters: only.pos = TRUE, min.pct = 0.1, logfc.threshold = 0.25, and an adjusted p-value cutoff of <0.05. The most significant DEGs were selected by sorting based on adjusted p-value. To generate cardiomyocyte only datasets, we further subclustered cells from clusters that expressed *TNNT2* and defined the cardiomyocyte subtypes as detailed in the main text. To visualize gene expression in two dimensions Uniform Manifold Approximation and Projection (UMAP) was used for dimensionality reduction. NKX2-5$^+$TBX3$^+$ (Nkx2-5 expression threshold: > 0, TBX3 expression threshold: > 0) and NKX2-5$^+$TBX3$^-$ (Nkx2-5 expression threshold: > 0, TBX3 expression threshold: = 0) cells were computational isolated from our HES2-derived BMP2 AVNLPC dataset to further validate our NKX2-5$^+$TBX3$^+$-based AVNLPC selection strategy used with the HES3-Nkx2-5$^{egfp/w}$ TBX3$^{tdtomato/w}$ reporter hPSC line. Analysis of DEGs confirmed enrichment of pacemaker genes in NKX2-5$^+$TBX3$^+$ cells while working cardiomyocyte genes were enriched in NKX2-5$^+$TBX3$^-$ cells (Table S6).

Gene Signature Scores

Gene signature scores were generated using UCell[105] based on the top 50 positive DEGs from the comparison groups. When there were fewer than 50 positive DEGs, all were included. The distribution of these signature scores was visualized using UMAP projections. For the comparison to the published fetal spatial MERFISH dataset (Farah et al.)[54] and adult AVN single nucleus dataset (Kanemaru et al.)[55] the top DEGs of each cell cluster of interest were identified in the supplementary data provided for each publication.

Gene ontology analysis

Database for Annotation, Visualization, and Integrated Discovery (DAVID) Bioinformatics Resources (version Dec. 2021, https://david.ncifcrf.gov/summary.jsp) was used to execute gene ontology analyses, focusing on biological processes (GOTERM_BP_all).

Integration of fetal and hPSC datasets

Fetal snRNA-seq and hPSC scRNA-seq datasets were separately normalized with SCtransform and clustered using Seurat. The two datasets were then concatenated to generate a merged gene expression matrix. IntegrateLayers (method = RPCA, k.anchor = 40) was then used to co-embed shared cell types. Dimensional reduction was then used to generate UMAPs for data visualization. Cell Clusters of the merged dataset were annotated based on the contribution of fetal cell types and gene expression patterns. Three clusters with contribution of fetal core AVN cells and expression of key AVN markers were identified and merged. Similarly, other clusters were annotated and merged as shown in Figure S5A.

Processing of Published sc/snRNA-seq Datasets

Published sc/snRNA-seq datasets from Ye et al., Li et al., Schmidt et al., Farah et al., and Kanemaru et al. were obtained from GEO or author databases.[40–42,54,55] Datasets were processed using the same pipeline as described in the respective publications, including quality filtering, normalization and clustering. AVC/AVN-like clusters were identified based on author annotations. Cardiomyocyte clusters were identified via expression of *TNNT2*.

Spearman correlation analysis

To evaluate the correlation between selected fetal (our dataset) or adult (Kanemaru et al.)[55] AVN cell types and hPSC-derived AVC/AVN-like cells we performed Spearman correlation analysis using the top 200 DEGs of each selected cell cluster from the reference dataset ranked by fold change. The following cell clusters were included in the analyses. For the fetal reference dataset, the Core AVN, Atrial Transition Zone (ATZ), Lower Nodal Bundle (LNB), Atrial, Ventricular, Endothelial, and Fibroblast clusters were included. For the adult reference dataset, the AVN, His Bundle and Atrial clusters were included. The correlation of the BMP2-AVNLPCs was analyzed for cardiomyocyte, endothelial and fibroblasts clusters as well as at higher resolution including the cardiomyocyte subtype clusters Core AVN, ATZ and LNB. In addition, correlation analysis using previously published datasets form hPSC-derived AVC/AVN-like cells (Ye et al, Li et al. Schmidt et al.)[40–42] was performed. For these datasets the AVC/AVN-like cell clusters were identified according to the authors annotations and included in the correlation analysis. For comparability all cardiomyocytes from our BMP2-AVNLPCs were included as one pooled AVN-like cluster when comparing to these other hPSC-datasets. Before calculating the Spearman correlation scores, duplicate features between the reference dataset DEG lists and genes not detected in the hPSC datasets were excluded.

Gene regulatory network analysis with pySCENIC

Raw expression matrices for the cardiomyocyte cluster from the *in vitro* scRNA-seq and fetal snRNA-seq datasets were used as input for pySCENIC (v0.12.1).[56,57] Genes not expressed in these clusters nor included in the cisTarget databases were removed prior to analysis. Gene regulatory networks (GRNs) were inferred independently for each dataset based on co-expression between transcription factors (TFs) and all expressed genes with GRNBoost2 using default parameters. Five runs of GRNBoost2 were performed, only retaining edges present in ≥60% of runs. Candidate regulatory modules were then generated using default parameters, only retaining activating regulons (positive Pearson correlation between TF and targets). Modules were pruned with cisTarget using the hg38 human database and default parameters, only retaining regulons with significant enrichment of TF motifs among targets. Regulon activity was quantified by per-cell gene signature scoring of targets with AUCell. Top regulons for each cardiomyocyte subcluster were found by ranking regulon specificity scores calculated from mean regulon activity within each cluster.[106] Upstream regulators of the top 10 Core AVN regulons were found with a 2-level recursive search for other regulons that contained the corresponding TFs regardless of cluster specificity. Fetal and *in vitro* GRNs were then merged by mean edge importance for visualization with force-directed graphs in Cytoscape (v3.10.4).[107]

Engineered Heart Tissues (EHTs)

Cardiomyocyte purification for EHTs

To generate eAVNT and eVT from the HES3-Nkx2-5$^{egfp/w}$ TBX3$^{tdtom/w}$ hPSC line SIRPA^{+}CD90^{-}NKX2-5^{+}TBX3^{+} AVNLPCs and SIRPA^{+}CD90^{-}NKX2-5^{+}TBX3^{-} VLCMs were isolated by FACS respectively and directly used for tissue generation. To generate eAVNT and eVT from the ESI017-ASAP1 hPSC line cardiomyocytes were enriched up to 80% by MACS using the PSC-Derived cardiomyocyte Isolation Kit (Miltenyi, 130-110-188). After the sort, the ESI017-ASAP1 AVNLPCs and VLCMs were cryopreserved as outlined above.

Cardiomyocyte thawing for EHTs

Cryopreserved vials of hPSC-derived cardiomyocytes were thawed in a 37°C water bath until a small ice pellet remained. Cells were gently resuspended in cardiac maintenance medium supplemented with 10 μg/mL DNase I (MilliporeSigma, 260913) and 10 μM ROCK inhibitor Y27632 (Selleckchem, S1049), transferred to a 15 mL conical tube, and washed with the same medium. Cells were centrifuged at 1200 rpm for 5 minutes, and this process was repeated twice. The final pellet was resuspended in cardiac maintenance medium containing 10 μM ROCK inhibitor and kept on ice until use.

Generation of EHTs

For the preparation of 3 mm engineered heart tissues, PDMS moulds were prepared by securing 210 μm diameter PDMS rods at either end of a PDMS well (4 mm long x 2 mm wide x 0.6 mm deep) to serve as anchors for the tissue. The mold dimensions were based on those of previously reported devices.[67,108–110] Cardiomyocytes were counted and seeded at a density of 160,500 cells per construct, along with commercially available cardiac fibroblasts (Lonza, CC-2904) at a density of 53,500 cells per construct. The cells were mixed and embedded in fibrin gels composed of fibrinogen (5 mg/mL; Sigma cat# F8630), aprotinin (0.00825 mg/mL; BioShop, APR600), thrombin (2 U/mL; Sigma-Aldrich, T7513), growth factor-reduced Matrigel (1 mg/mL), and Y-27632 (10 nm, STEMCELL, 72304), in DMEM. The cell suspension was seeded into the molds by pipetting with cold tips to prevent premature fibrin polymerization. The gels were incubated at 37°C for 1 hour to allow for polymerization, after which cardiac maintenance media (see above) was added. The tissues were cultured for 7 days to enable compaction, with the medium replaced every 2–3 days. Five days after seeding, the tissues were carefully detached from the walls of the molds using a 20-gauge needle to promote further compaction. Following an additional 5 days in culture (10 days total), the tissues were optically mapped.

Optical mapping of EHTs

Engineered heart tissues were mapped in 20% StemPro-34 diluted with IMDM supplemented with the above-described culture reagents. Tissues made with cells differentiated from the HES3-Nkx2-5$^{egfp/w}$ TBX3$^{tdtom/w}$ hPSC line were stained at 37°C, 5% CO_2 using the Fluo4 Membrane Potential Kit (ThermoFisher, F14201) according to the manufacturer's instructions. Fluorescence was recorded using a high-speed complementary metal-oxide semiconductor (CMOS) camera (Ultima-L, Scimedia) equipped with a 1cm sensor with a 100 x 100-pixel resolution, mounted on an MVX-10 Olympus fluorescence microscope with a 0.63–6.3X objective lens. Optical zoom was set at 4X, providing a 25 um/pixel spatial resolution for imaging. Recordings of 2–8 seconds were acquired at 500 or 1000 frames/s using the BrainVision software (Scimedia). The calcium indicator Fluo4 and the fluorescent voltage sensor ASAP1 were excited by a mercury arc source (X-Cite Exacte) with a 480-nm filter (Olympus U-MWIG2 filter cube). To detect fluorescence a 488-nm long pass filter was used. A heated plate (Olympus, MATS-U55S) was used to maintain the media/buffer at 37°C.

The tissues were electrically point-stimulated using a bipolar electrode made of two fine silver wires supported by a syringe mounted on a micromanipulator (World Precision Instruments) and connected to a Grass S88X stimulator. Tissues were paced at 2.5 Hz to determine conduction velocities. To test for the ability of the tissues to block the conduction of fast rates they were stimulated for 2 seconds at each frequency ranging from 2.5 Hz to 10 Hz. Decremental conduction properties were assessed using the following S1-S2 stimulation protocol: eight baseline stimuli (S1) were delivered at a fixed frequency of 2.5 Hz, followed by a premature stimulus (S2) applied at progressively higher frequencies ranging from 3 Hz to 10 Hz (Figure S6D). Electrical stimulation was applied via the pacing electrode at a fixed position at the bottom of the engineered tissue. For all tissues, action potentials were analyzed at a consistent region near the top of the tissue, approximately 2.5 mm from the stimulating electrode (Figure S6E). The S2-R2 latency was defined as the time interval between delivery of the S2 stimulus at the bottom of the tissue and the onset of the corresponding voltage or calcium transient (R2) at the top of the tissue.

Optical action potential characteristics (frequency, maximal upstroke velocity, and action potential duration) were analyzed using the Electromap Matlab software.[100] Activation maps were also created using Electromap. Conduction properties (conduction velocity, maximum capture rate, decremental conduction and the instance of the Wenckebach phenomenon) and diastolic depolarization were determined using the BrainVision software (Scimedia).

Guinea Pig Experiments

Guinea pig cryoinjury

Guinea pig experiments, including cardiac cryoinjury, cell injection, and *ex vivo* imaging, were performed as described in previous studies.[51,75,76] Briefly, animals were initially anesthetized with ketamine and xylazine, then maintained under anesthesia with 1.5% isoflurane and oxygen via intubation and mechanical ventilation (60 breaths per minute, tidal volume 5 mL/kg). A cryoinjury was induced by performing a left thoracotomy to expose the heart, followed by the application of a 5-mm diameter liquid nitrogen-cooled aluminum cryoprobe to the anterolateral left ventricle (LV) four times, each for 30 seconds.

Cardiomyocyte thawing for in vivo transplantation

Cryopreserved cardiomyocytes were thawed and prepared following previously established protocols to maximize survival during *in vivo* transplantation.[51,75,76] Briefly, cryopreserved vials of hPSC-derived cardiomyocytes were retrieved from a -150°C freezer and rapidly thawed in a 37°C water bath until a small ice pellet remained. Cells were gently resuspended and washed in pre-cooled 20% StemPro medium diluted in IMDM without Phenol Red (Thermo Fisher, 21056023), supplemented with 200 nM cyclosporine A/Sandimmune IV (Novartis, 00593257), 50 μM Pinacidil (Sigma, P154-100MG), and 10 μg/mL DNase I (MilliporeSigma, 260913). Cells were then pelleted by centrifugation at 1200 rpm for 10 minutes. The pellet was resuspended in pre-chilled IMDM without Phenol Red, supplemented with 200 nM cyclosporine A/Sandimmune IV, 50 μM Pinacidil, and 10 μg/mL DNase I, followed by centrifugation at 300 g for 10 minutes. This wash step was repeated twice. Finally, cells were resuspended in 100% cold Matrigel without Phenol Red (FisherScientific, CB40230C) supplemented with 200 nM cyclosporine A/Sandimmune IV and 50 μM Pinacidil to the target total injection volume of 250 μL. All pipetting steps were performed using cold, wide-bore pipette tips to minimize mechanical stress. Cell suspensions were kept on ice and sealed with parafilm to prevent contamination until transplantation.

Guinea pig cell injection

A second thoracotomy was conducted 10–14 days post-cryoinjury, during which 50–100 million hPSC-derived AVNLPCs or VLCMs were injected aiming to achieve grafts spanning from the scar into the healthy myocardium. Specifically, 2–3x 100 μL injections into the scar and border zone of the scar were performed. To prevent graft rejection, animals were treated with pharmacological immunosuppression starting 2 days before cell injection and continuing until the endpoint of the experiment. The immunosuppression regiment consisted of cyclosporine A/Sandimmune IV (15 mg/kg/day subcutaneously until day 7 post-transplant, followed by 7.5 mg/kg/day until day 15 post-transplant, and 5 mg/kg/day until the endpoint, Novartis, 00593257) and methylprednisolone (2 mg/kg/day intraperitoneally, Pfizer, DIN02367971).

Guinea pig ex vivo optical mapping

At 2–4 weeks post-transplantation, hearts were excised and mounted onto a Langendorff perfusion system. For *ex vivo* maintenance, the hearts were perfused with Working Heart Buffer containing 118 mM NaCl, 1.8 mM $CaCl_2$, 4.7 mM KCl, 1.2 mM $MgSO_4$, 1.2 mM KH_2PO_4, 25 mM $NaHCO_3$, 11 mM D-glucose, and 1 mM sodium pyruvate. The buffer was bubbled with 95% O_2/5% CO_2, adjusted to pH 7.35, and maintained at 37°C. To minimize motion artifact during *ex vivo* imaging, the buffer was supplemented with 10 μM blebbistatin (Cayman Chemical, 13186-50). A PowerLab 8/35 Data Acquisition System (AD Instruments) outfitted with a bioamplifier (Model ML136, AD Instruments), was used to record a pseudo-ECG via the Labchart software. The voltage-sensitive dye RH237 (Ex/Em: 532/700nm, ThermoFisher, S1109) was used to detect optical action potentials of the host. For the simultaneous recording of ASAP1 (hPSC-derived cardiomyocyte graft) and RH237 (guinea pig heart) fluorescent signals, a previously reported dual camera imaging system was used. This comprised of a collimating lens (25 mm, Navitar, N.A. 0.05, W.D. 10 mm) outfitted with a dichroic system (Photometrics DC2 dual-channel splitter) and two high-speed, high-sensitivity EMCCD cameras (Evolve128, Photometrics). The cameras were operated by the Metamorph software at 500 fps. Two LED spotlights (Mightex PLS-0470-030-15-S LEDs with Chroma ET470/40x filters) were used to excite the fluorescent signals. Prior to detection, the ASAP1 and RH237 fluorescent signals were separated by a dichroic mirror (643 nm) and filtered (530 ±20 nm and >705 nm, respectively).

The hearts were mapped at sinus rhythm and after the induction of an SAN/AVN block, which was triggered by adding methacholine (10 mg/mL, Sigma, A2251-25G) to the perfusate. Non-rhythmic beating was defined as spontaneous activation of the host via the graft in which the cycle length varied for the majority of the beats or the trace contained pauses or irregular bursts of activity. The hearts or cellular grafts were electrically point-stimulated using a bipolar electrode made of two fine silver wires (AWG#32) supported by a syringe mounted on a magnetic stand with a ball joint (World Precision Instruments) driven by the PowerLab system. Hearts/grafts were paced at 2.0 Hz to determine conduction velocities within the grafts. To test for the ability of grafts to block the conduction of fast rates hearts/grafts were paced with increasing frequencies ranging from 1 Hz to 8 Hz in 0.5Hz increments.

Raw data from the ASAP1, RH237, and ECG channels were processed using previously described Matlab scripts to generate Figures 7D–7G, 7L, and 7M.[51] Optical action potential characteristics, including frequency, maximum upstroke velocity, and action potential duration, as well as conduction velocity, were analyzed with Electromap software.[100] Activation maps were also created using Electromap. Activation maps of the whole hearts were derived from the RH237 signal. Activation maps of the grafts were derived from the ASAP1 signal. Maximum capture rates and optical action potential analysis for diastolic depolarization were performed using Metamorph software.

QUANTIFCATION AND STATISTICAL ANALYSIS

Data are presented as mean ± standard error of the mean (SEM). For all *in vitro* differentiations indicated samples size (n) represent biological replicates (independent differentiation experiments). For *in vivo* animal studies, experimental group size (n = animal numbers) was estimated based on power analyses using population variance in previous work. Animals were selected at random by a technician blinded to experimental treatment. Statistical analysis was performed using GraphPad Prism version 10.4.1 for macOS (www.graphpad.com). Datasets were assessed for normality using the Shapiro-Wilk test ($\alpha = 0.05$). For normally distributed data, the following statistical tests were employed: a two-sided unpaired Student's t-test for comparisons between two conditions, and one-way ANOVA with Bonferroni post hoc test for comparisons among multiple conditions. For datasets that did not pass the normality test, the following statistical test was used: Two-sided unpaired Mann-Whitney test. Results were considered statistically significant at $p < 0.05$ (*), $p < 0.01$ (**) and $p < 0.001$ (***). All sample sizes, statistical methods and statistical parameters, including p-values, are detailed in the respective figures and figure legends. In addition, Table S7 contains a detailed summary of data points, statistical analyses and p values presented in the figures. Due to the nature of the study, the experiments were not randomized and the investigators were not blinded to allocation during experiments and outcome assessment. Except for the animal experiments, no statistical methods were used to pre-determine sample sizes.